

# Fault and fracture distribution within a tight-gas sandstone reservoir: Mesaverde Group, Mamm Creek Field, Piceance Basin, Colorado, USA

Sait Baytok<sup>1\*</sup> and Matthew J. Pranter<sup>2</sup>

<sup>1</sup>Turkish Petroleum Corp. (TPAO), Söğütözü, 2180nd Avenue No. 86, 06100 Çankaya, Ankara, Turkey

<sup>2</sup>Department of Geological Sciences, University of Colorado Boulder, Colorado 80309, USA

\*Corresponding author (email: [sbaytok@tpao.gov.tr](mailto:sbaytok@tpao.gov.tr))

**ABSTRACT:** The distribution and orientation of faults, fracture intensity and seismic-reflection characteristics of the Mesaverde Group (Williams Fork and Iles formations) at Mamm Creek Field vary stratigraphically, and with lithology and depositional setting. For the Mesaverde Group, the occurrence of faults and natural fractures is important as they provide conduits for gas migration, and enhance the permeability and productivity of the tight-gas sandstones. The Upper Cretaceous Mesaverde Group represents fluvial, alluvial-plain, coastal-plain and shallow-marine depositional environments.

Structural interpretations based on three-dimensional (3D) seismic-amplitude data, ant-track (algorithm that enhances seismic discontinuities) seismic attributes and curvature attributes are utilized jointly to understand the complex fault characteristics of the Williams Fork Formation. This study reveals that the lowermost lower Williams Fork Formation is characterized by NNW- and east–west-trending small-scale thrust and normal faults. Study suggests that the uppermost lower Williams Fork Formation, and the middle and upper Williams Fork formations, exhibit NNE- and east–west-trending arrays of fault splays that terminate upwards and do not appear to displace the upper Williams Fork Formation. In the uppermost Williams Fork Formation and Ohio Creek Member, NNE-trending discontinuities are displaced by east–west-trending events and the east–west-trending events dominate.

Fracture analysis, based on borehole-image logs, together with ant-track and attenuation-related seismic attributes, illustrates the spatial variability of fracture intensity and lithological controls on fracture distribution. In general, higher fracture intensity occurs within the southern, southwestern and western portions of the field, and fracture intensity is greater within the fluvial sandstone deposits of the middle and upper Williams Fork formations. More than 90% of natural fractures occur in sandstones and siltstones. *In situ* stress analysis, based on induced-tensile fractures and borehole breakouts, indicates a NNW orientation of present-day maximum horizontal stress ( $S_{H_{max}}$ ), an approximate 20° rotation (in a clockwise direction) in the orientation of  $S_{H_{max}}$  with depth and an abrupt stress shift below the Williams Fork Formation within the Rollins Sandstone Member.

## INTRODUCTION

The Piceance Basin of NW Colorado produces natural gas from an interval of lenticular, relatively discontinuous, tight-gas fluvial sandstones of the Upper Cretaceous Mesaverde Group (Fig. 1). Through the US Department of Energy (DOE) Multiwell Experiment (MWX) project (1981–1988 at Rulison Field: Fig. 1), cores, borehole-image logs, well tests and other data indicated that the low-permeability sandstone reservoirs of the Williams Fork Formation were naturally fractured at depth (Lorenz 2003). The poor correlation between net pay and estimated ultimate recovery also suggests that fractures contribute to productivity. Since the 1980s, studies by Lorenz & Finley (1991), Grout & Verbeek (1992), Hoak & Klawitter (1997), Kuuskraa *et al.* (1997a, b),

Lorenz (1997), and others have focused on fracture characteristics and their controls on gas production. Decline in well productivity from 2.2×10<sup>9</sup> ft<sup>3</sup> (BCF (*billion cubic feet*)) of gas (wells drilled from 1996 to 2000) to 1BCF of gas (wells drilled from 2003 to 2005) per well shows the importance of additional studies to evaluate fracture characteristics, and their distribution and role in unconventional gas plays (Kuuskraa 2007).

This study explores the distribution and characteristics of fractures and faults and controls on fracture distribution through analysis of borehole images, three-dimensional (3D) seismic data, and relationships between seismic attributes and fracture intensity (Baytok 2010). The study area is located approximately 7.5 miles (12 km) SE of Rifle, Colorado (Figs 1 and 2). The dataset includes 10 borehole-image (Formation MicroImager (FMI))

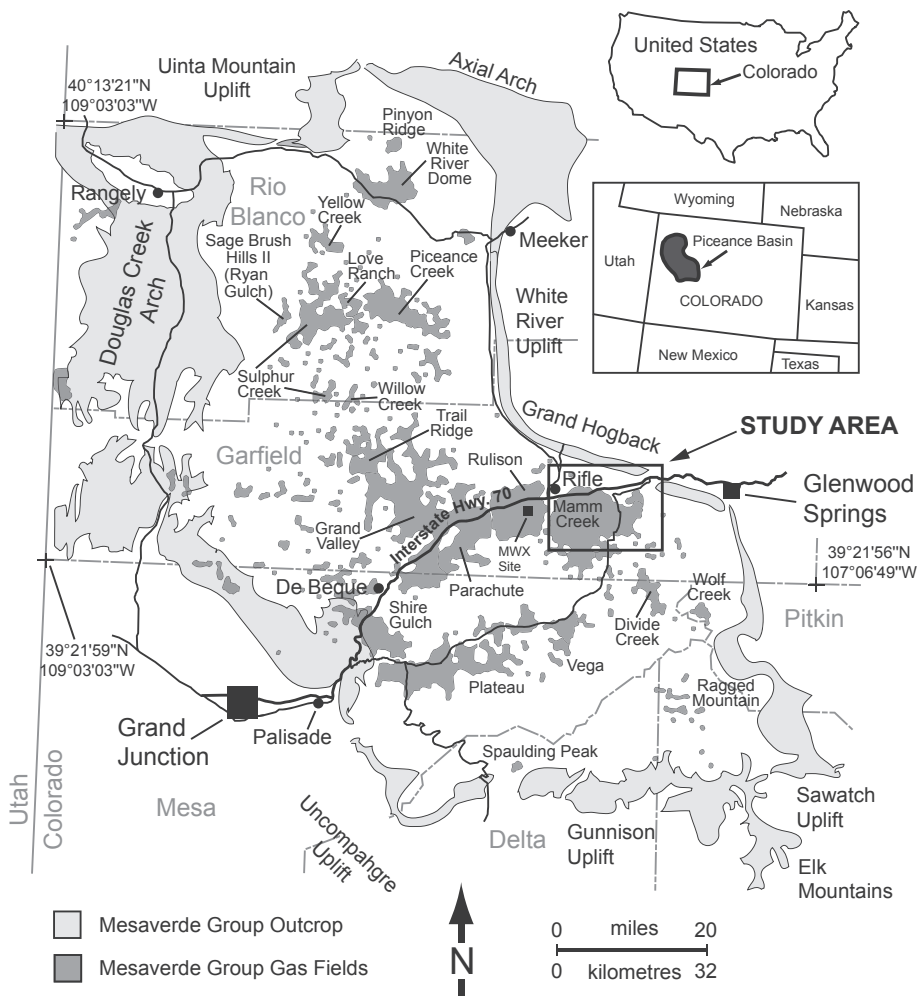


**Fig. 1.** Map of the Piceance Basin. Map shows the exposed Mesaverde outcrop along the margins of the basin (including the Williams Fork Formation) and the major Mesaverde Group gas fields in the basin. The study area is outlined. The MWX site can be seen. Modified from Hoak & Klawitter (1997) and Pranter *et al.* (2009).

logs, core (and associated data including FMI logs) from one well, a three component (3C), 3D seismic survey in depth and time domains, and well logs (gamma ray (GR), neutron porosity (NPHI) and density porosity (DPHI)) and formation tops for 617 wells (Fig. 2). Most wells in the area penetrate the Cretaceous Rollins Sandstone Member (stratigraphically below the Williams Fork Formation) and have a total vertical depth (TVD) range from 6700 to 9600 ft (2042–2926 m). The 3D seismic survey covers an area of approximately 48 miles<sup>2</sup> (125 km<sup>2</sup>), an inline length of 31 790 ft (9689.5 m), a cross-line length of 42 350 ft (12 908 m), and 110 ft (33.5 m) inline and cross-line spacing. Depth conversion of the seismic was conducted using interval velocities. The time and depth volumes have sample rates of 0.5 ms and 4 ft (1.2 m), respectively, and both surveys have the same XY Universal Transverse Mercator system co-ordinates and trace-bin geometry (Fig. 2). Acquisition parameters and the processing sequence of seismic data used in this study are given in Tables 1 and 2.

## GEOLOGICAL BACKGROUND

The Piceance Basin is an elongate, NW–SE-trending basin formed by Laramide tectonism from latest Cretaceous through to Palaeocene time. The basin has a highly asymmetrical profile with gently dipping western and southwestern flanks, and a steeply dipping eastern flank. Exposure of strata on the eastern flank of the basin is almost vertical at the Grand Hogback (Fig. 1), which is a steep Laramide monocline underlain by a low-angle basement-involved thrust fault (Tweto 1975; Grout *et al.*

1991). The Piceance Basin is bounded by the Uinta Mountain uplift on the NW, the Axial Arch on the north, the White River uplift on the east, the Elk Mountains and Sawatch uplift on the SE, the Gunnison uplift on the south, the Uncompahgre uplift on the SW, and the Douglas Creek Arch on the west (Fig. 1). The structural development of the Piceance Basin began near the end of the Cretaceous and continued during the Tertiary period, and was influenced by two major tectonic events: the Sevier Orogeny and the Laramide Orogeny (Johnson 1989; Grout *et al.* 1991). Even though both tectonic events played a role in the development of the Piceance Basin, the Laramide Orogeny formed the present shape and configuration of the Piceance Basin as one of a number of structural depressions in the Rocky Mountain region (Johnson 1989).

The stratigraphic nomenclature for the Mesaverde Group in the eastern and southeastern Piceance Basin (Carroll *et al.* 2004) is used herein (Fig. 3). In the eastern part of the Piceance Basin, the Mesaverde Group includes the Iles Formation, the Williams Fork Formation and the Ohio Creek Member. The lowermost part of the Mesaverde Group is the Iles Formation (also called the Mount Garfield Formation in the Grand Junction area), which comprises three regressive marine sandstone cycles (from base to top: the Corcoran, Cozzette and Rollins Sandstone members) separated by ‘tongues’ of the marine Mancos Shale. Hettinger & Kirschbaum (2002, 2003) described the three members of the Iles Formation as having been deposited in inner-shelf, deltaic, shoreface, estuarine and lower coastal-plain settings.

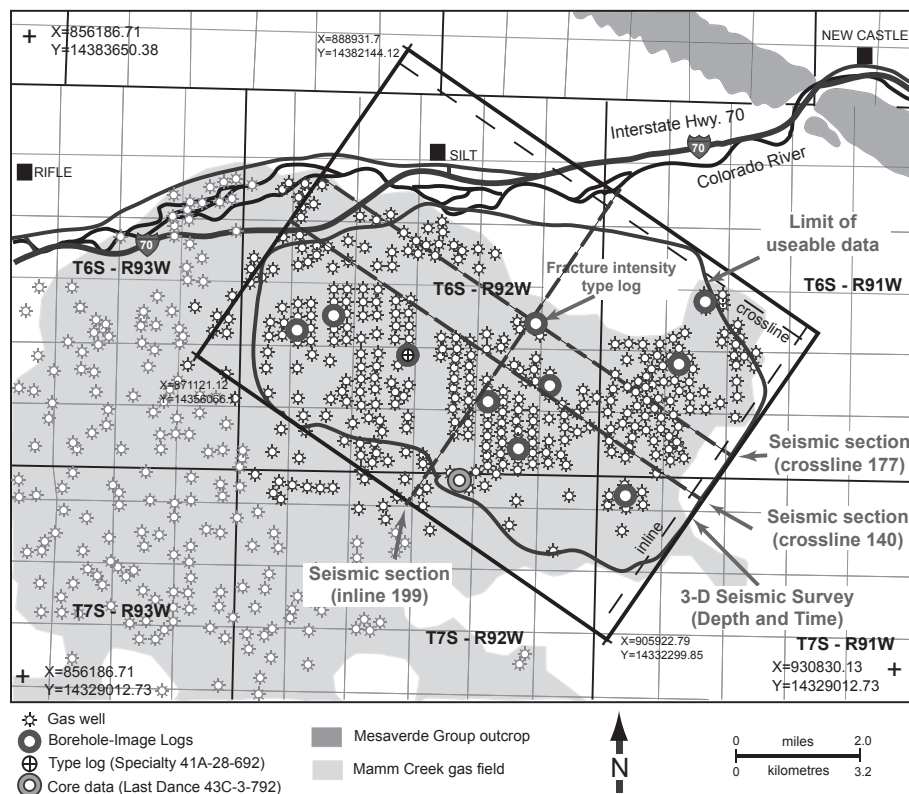


Fig. 2. Study area base map. The location of the base map is shown on Figure 1.

The Williams Fork Formation unconformably overlies the Iles Formation, and varies in thickness from approximately 5000 ft (1524 m) to 1200 ft (365 m) throughout the basin (Hettinger & Kirschbaum 2002, 2003). The thickness variation is thought to be due to the combination of a regional erosional surface at the top of the Williams Fork Formation and/or subsidence during deposition (Johnson & Roberts 2003; Cole & Cumella 2005). In the Piceance Basin, the Williams Fork Formation forms the main reservoir sandstones and was deposited in alluvial-plain, lower coastal-plain, and shallow-marine settings, and contains interbedded sandstone, shale and coal (Cole & Cumella 2005; Pranter *et al.* 2008; Shaak 2010). The individual sandstone reservoirs are 20–60 ft (6–18 m) in thickness, have porosity values from approximately 5% to in excess of 8% and permeability values of 0.01–0.1 mD (Pitman & Spencer 1984; Tremain 1993; Spencer 1996; Johnson & Roberts 2003). The Williams Fork Formation comprises (from stratigraphic base to top): (1) the Bowie Shale Member, which includes (from base to top) the Cameo-Wheeler coal zone, the South Canyon coal zone, the middle Sandstone and the upper Sandstone; (2) the Paonia Shale Member, which includes the Coal-Ridge coal zone; and (3) the undifferentiated middle and upper Williams Fork Formation (Figs 3 and 4) (Collins 1976; Hettinger & Kirschbaum 2002, 2003; Carroll *et al.* 2004). In the study area, the lower 1200–1500 ft (365–457 m) of the Williams Fork Formation consists of coal-bearing coastal-plain deposits, marine shale and marginal-marine sandstones of the Bowie Shale and Paonia Shale members that were deposited in inner-shelf, shoreface and coastal-plain settings (Hettinger & Kirschbaum 2003; Shaak 2010). The Bowie Shale Member ranges in thickness from 680 to 1000 ft (207–305 m), and consists of two superimposed coal-bearing coastal-plain stratigraphic units overlain by marine shale and marginal-marine sandstone (Collins 1976; Hettinger & Kirschbaum 2002, 2003; Shaak 2010). Collins (1976) named the two marginal-marine sandstones the middle and upper Sandstones, respectively. The middle and upper

Sandstones are only present in the easternmost part of the basin (Fig. 3). The Paonia Shale Member is 560 ft (170 m) in thickness and is characterized by coal-bearing coastal-plain deposits. The middle and upper intervals of the Williams Fork Formation combined are approximately 2000–4000 ft (610–1220 m) in thickness, and are characterized by fluvial deposits, conglomeratic sandstones, conglomerate, siltstone, minor shales and the lack of coal (Hettinger & Kirschbaum 2002, 2003; Pranter *et al.* 2008). In the upper Williams Fork Formation, a basin-wide thin (thickness of *c.* 20 ft (*c.* 6 m) and higher gamma-ray values) shale interval known as the upper Williams Fork Shale marker (UWFSM) is thought to be a top seal for vertical gas migration. The UWFSM is about 50 ft (15 m) below Price Coal. Price Coal is a thin coal (typically less than 5 ft (1.5 m)) and is present from the Parachute to the Mamm Creek fields. The UWFSM also has significance because it has a distinct seismic response over much of the Piceance Basin (Cole & Cumella 2005). In the study area, Price Coal can be thought of as a marker for the UWFSM. The uppermost 50–400 ft (15–122 m) of the Mesaverde Group is the Ohio Creek Member (also referred to as the Ohio Creek Conglomerate elsewhere), which consists of kaolinite-rich beds of sandstone, conglomeratic sandstone and conglomerate of fluvial origin (Johnson & May 1980; Hettinger & Kirschbaum 2002, 2003; Johnson & Flores 2003).

Fracture formation has been related to high pore-fluid pressure that developed during hydrocarbon generation, and to tectonic stress associated with uplift and erosion (Pitman & Sprunt 1986). Numerous studies in the central and eastern Piceance Basin relate natural fractures, regional structure and fault characteristics to gas production in the Williams Fork Formation. Lorenz & Finley (1991) identified a regional set of WNW extension fractures as an example of load-parallel extension fracturing and basinwide dilatancy at depth, under conditions of high pore pressure and anisotropic horizontal stress. Fracture height and spacing are highly variable, and fractures occur frequently in sandstones and siltstones (more than 95% in core)

**Table 1.** Gibson Gulch 3C survey acquisition parameters

Survey name: Gibson Gulch 3C  
 Township/range: Piceance Basin, Garfield County, COLORADO  
 Coverage: 24 sq miles Survey type: Slant – 26.565 Fractionated: Yes

**Acquisition parameters****Recording**

No. of sample intervals: 1800  
 Record: 8.0 s

**Geometry (all distances are either parallel or perpendicular to receiver lines)**

Source: 220 ft Receiver interval: 220 ft Receiver line interval: 1100 ft  
 Source Line: 1100 ft Receiver line: ENE

**Patch**

No. of receivers/line: 100 Roll inline: Yes  
 No. of receiver lines: 18

**Source and receiver (source counts are estimates only)**

Vibrator points: 2281 Buggy holes: 182  
 Heliportable holes: 0 Conventional: 0

**Source parameters (mixed)****Dynamite**

Hole depth: 60 m  
 Charge size: 20 kg

**Vibroseis**

Vibrator type: buggy No. of vibrators: 4 Vibrator weight: 50000 lbs  
 Sweep type: Non-linear Start taper: 0.5 s No. of sweeps: 7  
 End taper: 0.3 s Sweep length: 14 s Minimum sweep: 6.0 Hz  
 Sweep listen: 8 s Maximum sweep: 112.0 Hz

**Attributes**

Nominal fold: 90 Inline offset: 10890 ft  
 Inline fold: 10.0 Cross-line offset: 9350 ft  
 Cross-line fold: 9.0 Maximum: 14353 ft

Inline fold taper: 4125 ft Inline patch size: 18700 ft  
 Cross-line Fold Taper: 4895 ft Cross-line patch size: 21780 ft

Inline fold rate: 24.0 fold/line Inline/cross-line ratio: 86%  
 Cross-line fold rate: 20.2 fold/line Patch channels: 1800

**Source density design:** 115/sq. mile

**Receiver density design:** 115/sq. mile

and commonly terminate vertically at lithological boundaries (Lorenz & Finley 1989, 1991; Northrop & Frohne 1990). Fracture sets and areas of enhanced permeability within the Williams Fork Formation have also been linked to basement-involved thrust faults (Verbeek & Grout 1984; Grout & Verbeek 1992). In a study of structural-related production trends, Hoak & Klawitter (1997) suggested that basement-involved thrust faults terminate up-section in the coals and fluvial sandstones of the Mesaverde Group, and produce fracture-related permeability at fault tip-line terminations. Hoak & Klawitter (1997) also interpreted intense thrusting in the eastern Piceance Basin with a significant component of Mancos-level detachment on the faults. In contrast, Cumella & Ostby (2003) suggested a left-lateral transpressional structural style based on seismic data in the Parachute and Rulison fields (Fig. 1). They interpreted left-lateral, near-vertical faults trending approximately N45°, an eastwards rise of the Williams Fork Formation towards the Mamm Creek Field, abrupt thickness changes in the Cameo-Wheeler coal zone near faults that could indicate structural growth during Cameo deposition and major fault zones in the Mesaverde Group that are related to deep-seated faults. The present-day maximum horizontal, compressive-stress orientation has been interpreted to range from N52°W to N80°W in the paludal interval, from N58°W to N88°W in the coastal interval

and from N55°E to N103°E in the fluvial interval (Nelson 2003).

**METHODS****1D fracture analysis**

Well-based fracture analysis was based on 10 resistivity-based borehole-image logs. Ten borehole-image (Formation MicroImager) logs were a primary source of fracture information. Core (and associated data) from one well (Last Dance 43C-3-792) were used to evaluate the reliability of borehole images, and to compare fracture occurrence to lithology and deposit type (Fig. 2). The borehole-image data and associated fracture interpretations, including fracture type, classification, description (open, sealed, etc.), apparent dip and apparent azimuth, were used together with depth information to conduct further analyses.

Borehole-image-based fracture interpretations were used to generate fracture-intensity logs. Fracture-intensity logs show the density of fractures per unit length, and were used to investigate the relationships between lithology, architectural elements and fracture intensity, and for seismic analysis of fractures. Even though seismic reflection data alone may not quantify fracture properties, highly fractured areas (fracture sweet spots) can be identified indirectly by measuring certain seismic attributes such as velocity, impedance, AVO (amplitude v. offset), dip magnitude, dip azimuth, coherence, volumetric curvature and attenuation-related attributes. Cumulative fracture-intensity logs were also generated and were useful to divide the reservoir into mechanical zones. Fracture orientations of conductive and non-conductive (resistive) fractures, as well as measured dip-angle and dip-azimuth values from borehole-image logs, were displayed on equal-angle (Schmidt) stereographic-net projections and rose diagrams (dip azimuth and strike azimuth). Borehole-image logs were also used to evaluate present-day *in situ* stress directions on the basis of wellbore failures, which comprise both borehole breakouts as compressive failures and drilling-induced tensile fractures as tensile failures (Moos & Zoback 1990; Tezuka *et al.* 2002).

To examine the controls on fracture distribution, lithology and architectural-element logs were created for the 10 wells with borehole-image logs. Four lithologies were determined based on gamma-ray, density-porosity and neutron-porosity logs using the following criteria: (1) clean sandstone <70 API gamma-ray cut-off; (2) shaley sandstone ≥70 API and ≤96 API gamma-ray cut-off; (3) shale >96 API gamma-ray cut-off; and (4) coal ≤96 API gamma-ray cut-off, and >0.25 for density-porosity and neutron-porosity readings. The criteria used to interpret architectural-element logs are: (1) channel bars and point bars ≤96 API on gamma-ray log, 'upwards-fining' gamma-ray log signature, 0.05–0.25 density-porosity log values, sharp base and thickness values of 2–30 ft (*c.* 0.5–9 m); (2) crevasse splay ≤96 API gamma-ray cut-off, 'upwards-coarsening' gamma-ray log signature, <0.05 density-porosity log response and thickness values of approximately 1–15 ft (*c.* 0.3–4.5 m); (3) floodplain >96 API gamma-ray cut-off; and (4) coal ≤96 API gamma-ray cut-off and >0.25 density- and neutron-porosity log values. After creating lithology and architectural-element logs, further analyses were conducted to investigate the occurrence and amount of fractures by lithology and architectural element.

**3D seismic analysis of faults and fractures**

Seismic horizon interpretation was conducted using a depth seismic volume, whereas structural interpretation was performed

**Table 2.** Gibson Gulch 3C survey processing sequence (processed by WesternGeco Geophysical Services)

PROCESSING SEQUENCE
<b>P-Wave Pre-Migration Processing</b>
<ul style="list-style-type: none"> <li>• Reformat data to processing format</li> <li>• Input shot data with geometry in the trace headers or input field tapes</li> <li>• Load data to disk/display shot records and edit bad traces</li> <li>• Define geometry – compute field static corrections, if not supplied</li> <li>• Geometry quality control</li> <li>• Instruments and sensors de-phasing, if necessary</li> <li>• Resample to 4 ms as needed</li> <li>• First break picking and Miser reflection statics</li> <li>• Spherical Divergence Correction</li> <li>• Surface Consistent Deconvolution</li> <li>• Frequency-Dependent Noise Attenuation (FDNA) – evaluate and apply if needed</li> <li>• Noise Attenuation: (ANA, SWATT, other) (based on testing)</li> <li>• Zone Anomaly Processor to remove noise (ZAP)</li> <li>• Surface Consistent Amplitude Correction (SCAC)</li> <li>• Offset Relative Amplitude Corrections (ORAAC) if needed</li> <li>• Residual Statics and velocity analysis (maximum of two passes)</li> <li>• Surface Consistent Amplitude Correction (SCAC) – if required</li> <li>• Additional noise attenuation, if necessary (AANA, SWATT, other)</li> <li>• Prepare data for migration (filtering, remove scaling, as required)</li> </ul>
<b>Isotropic Pre-Stack Kirchhoff Time Migration</b>
<ul style="list-style-type: none"> <li>• Derive a Kirchhoff PSTM velocity field on a ½ square mile grid by target 3D migrations onto full inline and cross-line profiles. Velocity analyses to be picked in migrated space on this grid.</li> <li>• Full 3D Isotropic Kirchhoff PSTM including curved rays <ul style="list-style-type: none"> <li>- Input approximately 26sq. miles and output approximately 26sq. miles</li> <li>- Grid – 110×110ft input and output</li> <li>- Other parameters to be determined through testing</li> <li>- VTI parameter estimation and correction available as needed</li> </ul> </li> <li>• RAAC (Offset Dependent Residual Amplitude Compensation)</li> <li>• Residual Velocity Analyses on ½ mile grid, including eta scans if needed</li> <li>• NMO (fourth-order correction as required)</li> <li>• Final full fold stack – unscaled to tape</li> <li>• Final full fold stack with post stack noise attenuation and filters – unscaled and scaled to tape</li> <li>• Final NMO-corrected gathers to tape</li> </ul>

using both time and depth seismic volumes (Fig. 5). Seven key stratigraphic surfaces were interpreted in the study area (from stratigraphic top to base): (1) top Mesaverde Group (also referred to as top Ohio Creek Member); (2) top Williams Fork Formation (also referred to as base Ohio Creek Member); (3) Price Coal; (4) top Paonia Shale Member (also referred to as base middle Williams Fork Formation); (5) middle Sandstone; (6) Cameo-Wheeler coal zone; and (7) Rollins Sandstone Member (Fig. 5). Each stratigraphic surface and interval differs in regard to reflection configuration, reflection strength, and reflection continuity.

Evaluation of the occurrence, type, distribution and orientation of faults was conducted using 3D seismic P-wave data with curvature and ant-track (algorithm that enhances seismic discontinuities) attributes. A combination of both manual and auto-track interpretation was used with an integrated workflow that merged the analysis of the seismic-amplitude and ant-track attribute volumes. The ant-tracking algorithm is developed based on the idea of ant colony systems to highlight discontinuities in seismic data. The ant-tracker uses the principles of swarm intelligence, which describes the collective behaviour of social insects; for example, how ants find the shortest path between the nest and a food by communicating via a chemical

substance (Pedersen *et al.* 2002). Intelligent agents, also referred as ‘artificial ants’, trace or extract discontinuous features in a 3D seismic-derived, edge-detection attribute volume (such as chaos, variance or coherence attributes). Non-structural features such as noise and channels are less likely to be highlighted with the ant-tracking algorithm because they commonly exhibit more spatially random characteristics with relatively lower continuity.

The ant-track workflow includes three main steps: (1) seismic conditioning (structural smoothing) and generation of an edge-detection volume; (2) application of ant-tracking on the edge-detection volume to generate an ant-track volume to highlight and extract potential faults; and (3) interactive interpretation so that the faults can be evaluated, edited and filtered to obtain a final fault interpretation. Seismic conditioning improves data signal-to-noise ratio. Structural smoothing uses principle component dip and azimuth computation to determine the local structure; then, Gaussian smoothing is applied parallel to the orientation of the structure so as to enhance the results of edge-detection algorithms (e.g. variance, chaos) to better image spatial discontinuities in the seismic data. It is valuable to apply structural smoothing as it helps edge detection to capture discontinuities. Ant-tracking creates a new fault attribute that highlights fault-surface features. Interactive interpretation involves traditional 3D seismic interpretation and auto-tracking methods or automatic-fault extraction. This step is necessary to validate extracted surfaces as surfaces that are not faults can also be highlighted and extracted (Pedersen *et al.* 2002).

The detection of subsurface fractures and the estimation of fracture parameters from seismic data have a great importance in hydrocarbon recovery because significant amounts of hydrocarbons are trapped in tight reservoirs, where natural fractures have great impact on production (Sava *et al.* 2007). Although borehole-image logs, cores, outcrops and conventional well logs provide direct observations of fractures and fracture properties, they commonly do not provide adequate information about how fracture orientation, intensity and distribution change spatially with respect to distance from the wellbore. In order to investigate fracture intensity between wells, seismic attributes were used. Seismic-based fracture analysis involved comparison of ant-track and attenuation-related seismic attributes with fracture-intensity logs generated from borehole-image-log interpretations. Detail regarding the ant-track methodology used for fracture analysis is described by Baytok (2010). In addition to ant-track seismic attributes, frequency-dependent attenuation of amplitudes can be used as a fracture indicator (Najmuddin 2001). Haugen & Schoenberg (2000) discussed scattering caused by fractures and its relationship to wavelength. Schoenberg & Douma (1988) analysed the preferential attenuation of higher-frequency seismic amplitudes by fractures, and Liu *et al.* (1997) and Gibson *et al.* (2000) showed fracture-generated diffraction using synthetic seismic data derived from theoretical and physical models. The  $t^*$  attenuation attribute is based on P-wave seismic frequency data and is used to delineate fractures that can attenuate higher frequencies (Najmuddin 2003). The  $t^*$  attribute was evaluated as an additional qualitative attribute for fracture intensity. It is suggested by Najmuddin (2003) that higher  $t^*$  values indicate higher fracture intensity, larger thickness of the fractured layer or a combination of the two. This fracture indicator produces a qualitative attribute to indicate intensely fractured areas (production sweet spots). However, the  $t^*$  attribute does not promise to give a quantitative measure of the number of fractures (Najmuddin 2001). The  $t^*$  parameter calculated from seismic data measures the change in the frequency spectra using a small time window above and below the fractured layer. In order to calculate  $t^*$  values, amplitude values related to specific frequencies from the spectra below and above are used in the equation. Najmuddin’s

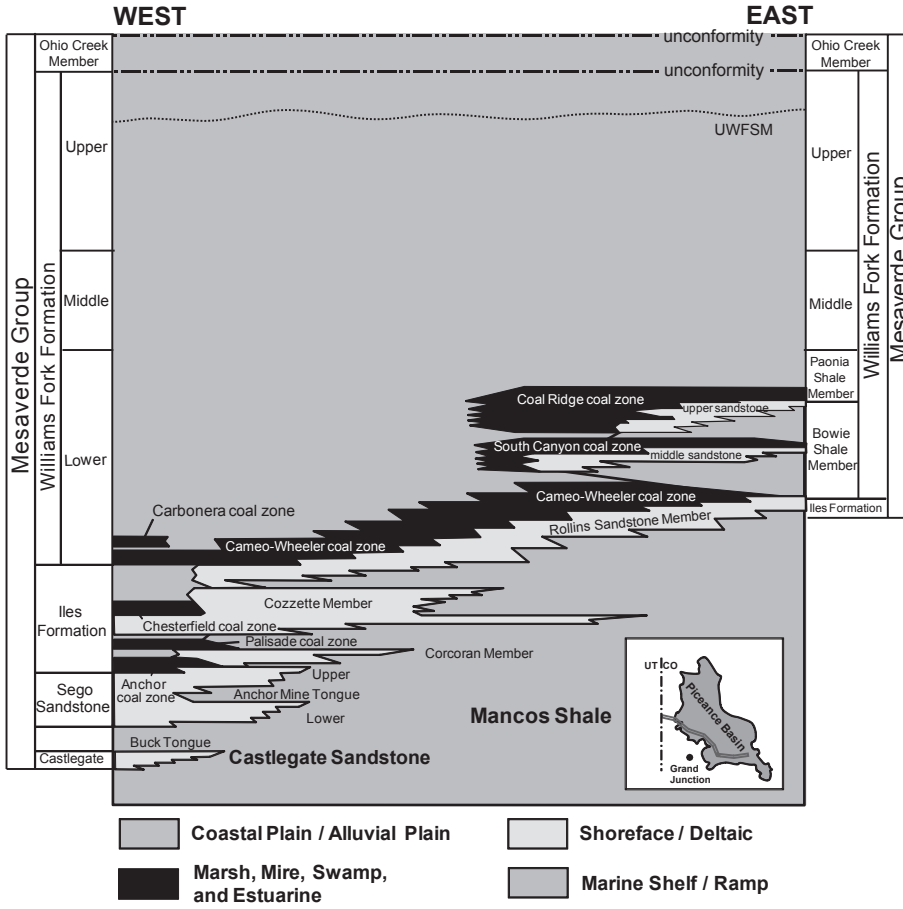


**Fig. 3.** Cross-section showing the stratigraphic nomenclature for the SE Piceance Basin. Modified from Carroll *et al.* (2004). The thickest portion of the basin is to the north of the cross-section.

(2001) equation for  $t^*$  is derived from Carmichael (1989), which is  $A(f, X) = G S(f) R(f) \exp(-\alpha X f)$ . In this equation  $G$  represents the geometrical spreading,  $S(f)$  represents the source function,  $R(f)$  represents the receiver function and  $-\alpha X$  substitutes for  $t^*$  (Najmuddin 2001). For a specific travel time, if  $A_{Abv}$  is the time window above,  $A_{Blw}$  is the one below, and  $f_{High}$  and  $f_{Low}$  are the high and low frequencies, the equation can be written as:

$$A_{Abv}(f, X) = G S_{Abv}(f) R_{Abv}(f) \exp(f t_{Abv}^*)$$

(represents the time window above the fractured layer)

$$A_{Blw}(f, X) = G S_{Blw}(f) R_{Blw}(f) \exp(f t_{Blw}^*)$$

(represents the time window below the fractured layer)

$$\ln(A_{Abv}) = \ln(G) + \ln R(f) + \ln S(f) + (t_{Abv}^*)f$$

$$\ln(A_{Blw}) = \ln(G) + \ln R(f) + \ln S(f) + (t_{Blw}^*)f$$

$$\ln(A_{Abv} / A_{Blw}) = \ln(G/G) + \ln(R(f)/R(f)) + \ln(S(f)/S(f)) + (t_{Abv}^* - t_{Blw}^*)f$$

In the final equation above, it is assumed that  $G$  and  $S(f)$  are the same for the two windows in the same trace. This leads to:

$$\ln(A_{Abv} / A_{Blw}) = (t_{Abv}^* - t_{Blw}^*)f$$

For the high ' $f_{High}$ ' and low ' $f_{Low}$ ' frequencies:

$$\ln(A_{Abv} / A_{Blw}) (at f_{High}) = (t_{Abv}^* - t_{Blw}^*)f_{High}$$

$$\ln(A_{Abv} / A_{Blw}) (at f_{Low}) = (t_{Abv}^* - t_{Blw}^*)f_{Low}$$

$$\ln(A_{Abv} / A_{Blw}) (at f_{Low}) - \ln(A_{Abv} / A_{Blw}) (at f_{High}) = (t_{Abv}^* - t_{Blw}^*)(f_{High} - f_{Low})$$

or

$$t^* = (t_{Abv}^* - t_{Blw}^*) = [\ln(A_{Abv} / A_{Blw}) (at f_{High}) - \ln(A_{Abv} / A_{Blw}) (at f_{Low})] / (f_{High} - f_{Low})$$

To compute a  $t^*$  attribute volume, a high- and low-frequency parameter selection is required, as well as a number of cycles, which determines the length of the extraction window. The high- and low-frequency values were selected with as much separation as possible within the dominant bandwidth of the data: 13 and 24 Hz were chosen for the low- and high-frequency parameters, respectively, with the number of cycles set at 2.0, after careful inspection of the frequency spectra above and below the target. It should be noted that noise in the data may cause some error in the  $t^*$  values because of its significant effect on the frequency content. The noise content of seismic data is assumed to be reasonably good due to the processing sequence, which includes steps for noise reduction (Table 1).

To compare the seismic attributes and fracture-intensity logs, as the seismic and well data are at different scales, the seismic

*Fault and fracture distribution within tight-gas sands*

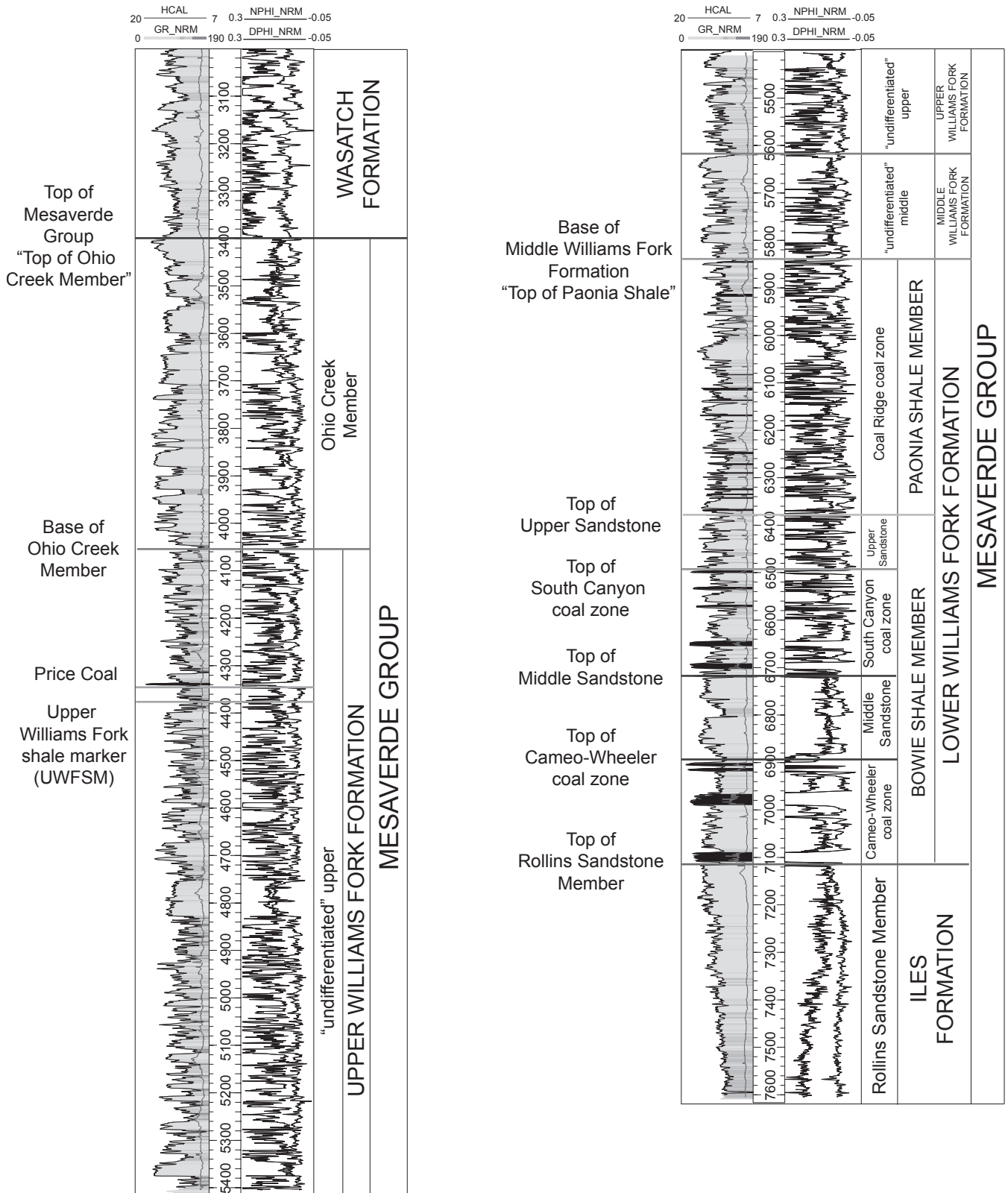


**Fig. 4.** Type log for the Mesaverde Group at the Mamm Creek Field (see Fig. 2 for the location). The interval comprises the Rollins Sandstone Member to the top of the Mesaverde Group. Measured depth units are in feet.

attributes were resampled into a 3D reservoir model grid of the area, and the fracture-intensity logs were up-scaled to the resolution of the grid. For the 3D reservoir model grid, different layering of 5, 10, 25, 50 and 100 ft (1.5, 3, 7.5, 15 and 30 m) were examined to find the optimal size of layering, and the

110×110×50 ft cell size was determined to be optimal. The seismic attribute was sampled into the 3D grid by assigning an attribute value to each cell using an intersecting method with arithmetic averaging in which all seismic cells intersecting the reservoir model grid cell contribute to the average. To upscale

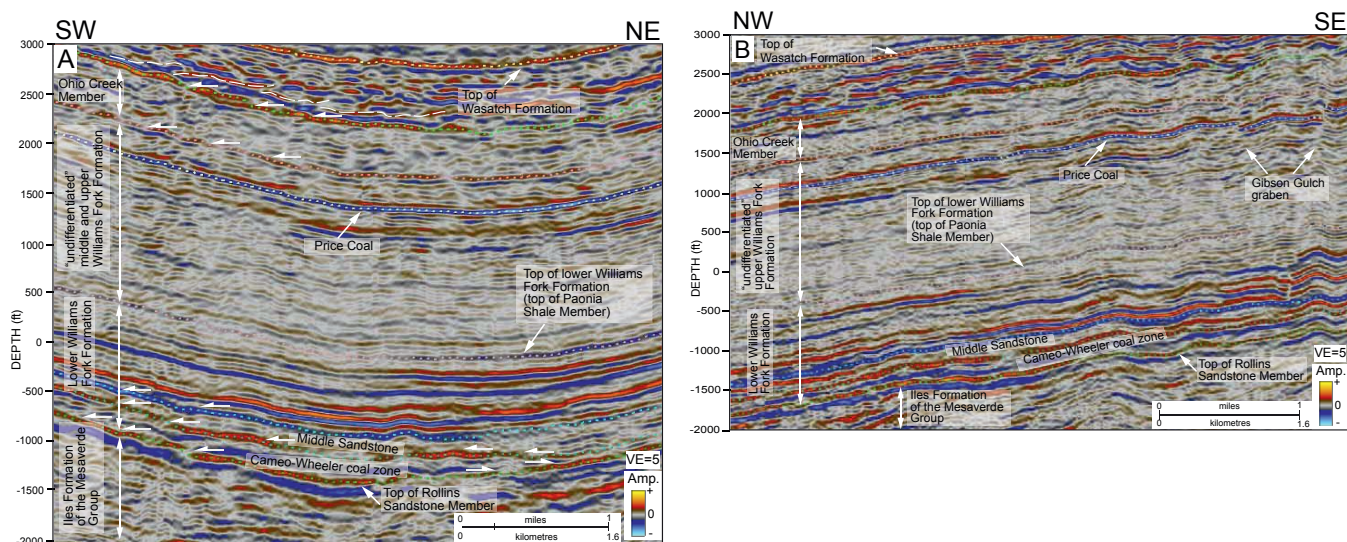


**Fig. 5.** (a) Seismic inline (inline 199) and (b) seismic cross-line (cross-line 140) through the seismic amplitude data showing reflection strength, reflection continuity and reflection configuration for each stratigraphic unit within the Mesaverde Group. The locations of the seismic sections are shown in Figure 2.

fracture-intensity logs, each reservoir grid cell that the well penetrates was assigned a log value based on the arithmetic average of log values that fall within the cell. After resampling and upscaling, the correlation was made between the attribute value and the log value for the cells along the wellbore.

## RESULTS

### 1D fracture intensity and distribution

**Fracture types.** Based on borehole-image data and interpretations, approximately 1634 natural fractures were categorized into: (1) conductive ( $N=1148$ ); and (2) resistive (non-conductive 'healed' or 'filled';  $N=486$ ) fractures. Conductive fractures appear as dark traces on electrical borehole-image logs and exhibit low resistivity because they are either (i) open and filled with a low-resistivity fluid of drilling mud; or (ii) are shale-filled fractures (Hurley 2004). Resistive fractures appear as light or white traces on electrical borehole-image logs and are commonly filled/cemented by calcite, anhydrite or quartz (Hurley 2004). Resistive fractures can act as permeability barriers within the reservoir and have a minimum contribution to production. Resistive fractures exhibit different characteristics in comparison to conductive (open) fractures; hence, they should be modelled and analysed separately. The occurrence of conductive fractures v. resistive fractures shows no apparent relationship in terms of depositional characteristics (fluvial v. marine) and depth. The data show that both resistive and conductive fractures can occur in any interval regardless of depositional environment.

**Fracture intensity.** Fracture-intensity logs and maps show how the distribution of fractures varies spatially (Figs 6 and 7). For the stratigraphic interval from approximately the Price Coal through to the Rollins Sandstone Member, the number of fractures, well to well, differs by as much as one order of magnitude (Fig. 7: low,  $N=30$ ; high,  $N=338$ ; mean,  $N=163$ ). Fractures are nearly vertical and dominantly strike WNW, parallel to the present-day *in situ* maximum, horizontal, compressive stress ( $S_{H_{max}}$ ). Sixty per cent of natural fractures are interpreted as being lithologically bound, and terminate against minor lithological boundaries within the reservoir sandstones and against shale that bounds the reservoir. More than 90% of natural fractures occur in sandstones and siltstones

(Fig. 8). However, a few natural fractures are observed in shale; those are mostly low-angle resistive fractures and some of them strike in a different orientation from that of  $S_{H_{max}}$  (S. D. Sturm 2010 pers. comm.). The origin of this fracture set is difficult to determine and might be related to a different stress field. Fracture occurrences, conductive v. resistive, show no apparent relationship regarding the depositional environment (fluvial v. marine) and depth. Seventy per cent of natural fractures occur in fluvial v. 30% in marine; however, it is difficult to draw a conclusion that the depositional environment, which controls the lithological variability, has primary control on fracture occurrences owing to the limited well depths. Only one well penetrates deep enough to have fracture data in the Cozzette and Corcoran marine sandstone intervals. The interval of electrical borehole-image log data covers only the marine units of the upper sandstone, middle sandstone and Rollins Sandstone Member of the Iles Formation (Fig. 3). The percentage of fractures in point bars, channel bars and crevasse splays does not vary significantly. Resistive fractures occur less in channel bars of the middle and upper Williams Fork Formation than in point bars and crevasse splays of the lower Williams Fork Formation (Fig. 9).

**Fracture orientations.** Conductive fractures exhibit a consistent strike of  $N45^{\circ}W$ , which is parallel to  $S_{H_{min}}$ , and have a mean dip of  $74^{\circ}$ . Resistive fracture strike orientation ranges from  $N45^{\circ}W$  to  $N80^{\circ}W$ ; however, NNE-striking resistive fractures are also present. A consistent NNW orientation for  $S_{H_{max}}$  is also evident from both induced-tensile fractures and borehole breakouts. Induced-tensile fractures have a strike orientation of NNW, whereas borehole breakouts form perpendicular to this orientation and are an indicator of minimum horizontal compressive stress ( $S_{H_{min}}$ ). Induced-tensile fractures and borehole breakouts are observed throughout the entire interval from 4000 to 8400 ft (1220–2560 m) of the image data for all 10 wells. Furthermore, dip azimuth values reveal a rotation of the axes of horizontal stresses along the well trajectory with depth. The axis of maximum horizontal stress from 4000 to 7200 ft (1220–2195 m) exhibits about  $20^{\circ}$  of rotation in a clockwise direction; however, there is approximately a  $20^{\circ}$  sudden counterclockwise shift in the rotation of stresses at about 7200 ft (2195 m), where the Rollins Sandstone Member of the Iles Formation exists. Below a

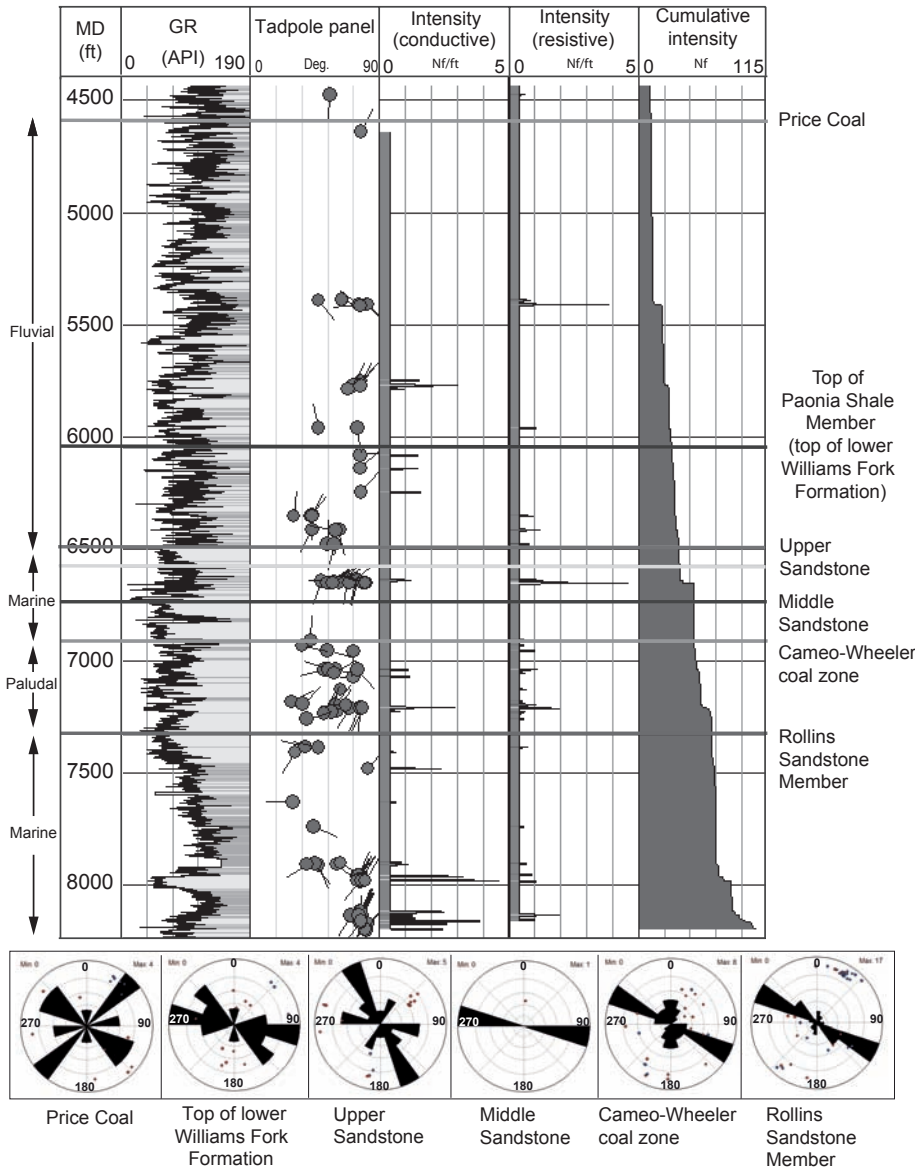


**Fig. 6.** Fracture-intensity type log for well BBC 42B-23-692 (see Fig. 2 for the location). Fracture-intensity logs were generated for conductive and resistive fractures using a 5 ft (1.5 m) window. The units on intensity tracks show the number of fractures per unit length and the total number of fractures from top on cumulative intensity track.

depth of 7200 ft (2195 m), a similar clockwise rotation change is observed. Such information may be useful in designing reservoir stimulation and fluid-flow simulation of sandstone reservoirs of the Williams Fork Formation; however, the real cause of this change is not clearly understood. It could follow from a different stress state at this depth.

Marine sandstone reservoirs of the Mesaverde Group are more laterally continuous and have more uniform internal characteristics, reflecting few internal discontinuities (Lorenz & Finley 1989). Conductive fractures within marine intervals of the Rollins Sandstone Member, the upper Sandstone and the middle Sandstone, commonly strike WNW. The distribution of these fractures is irregular, showing swarms of fractures in some wells along with unfractured and/or less fractured intervals. Resistive fractures also occur within the marine intervals, although less frequently than conductive fractures. The strike orientation of resistive fractures varies and their distribution is irregular. Regardless of whether a fracture is conductive or not, fractures occur in two sets: one set belonging to the regional system and striking WNW; and another less common set that strikes NNE. Typically, conductive fractures strike NNW, lie parallel to  $S_{H_{max}}$ , and are greater

in quantity and possibly more permeable (open, larger aperture, etc.) than resistive fractures.

Fluvial sandstone reservoirs of the Mesaverde Group differ significantly from marine sandstone reservoirs. Fluvial reservoirs are lenticular in shape, are often discontinuous, and contain internal lithological heterogeneities in terms of grain size, sedimentary structure and permeability (Pranter *et al.* 2007, 2008, 2009; Pranter & Sommer 2011). Because connectivity and internal heterogeneity of the Mesaverde fluvial sandstone reservoirs vary, poor communication may exist among fractures. Fractures within fluvial sandstone reservoirs provide considerable enhancement in permeability; thus, higher fracture-related productivity. Conductive fractures within these reservoirs exhibit dominant WNW fracture orientation; however, resistive-fracture strike varies within this interval as in the marine interval.

The Cameo-Wheeler coal zone interval exhibits similar kinds of reservoirs as in the fluvial interval, except that this interval differs with the presence of thick coal layers. Lorenz & Finley (1989) suggested that coal-derived fluids and gases within the paludal interval produced compaction, secondary porosity, and tertiary carbonate and quartz cement. Borehole-image logs indicate a higher number of resistive (healed/cemented) fractures in

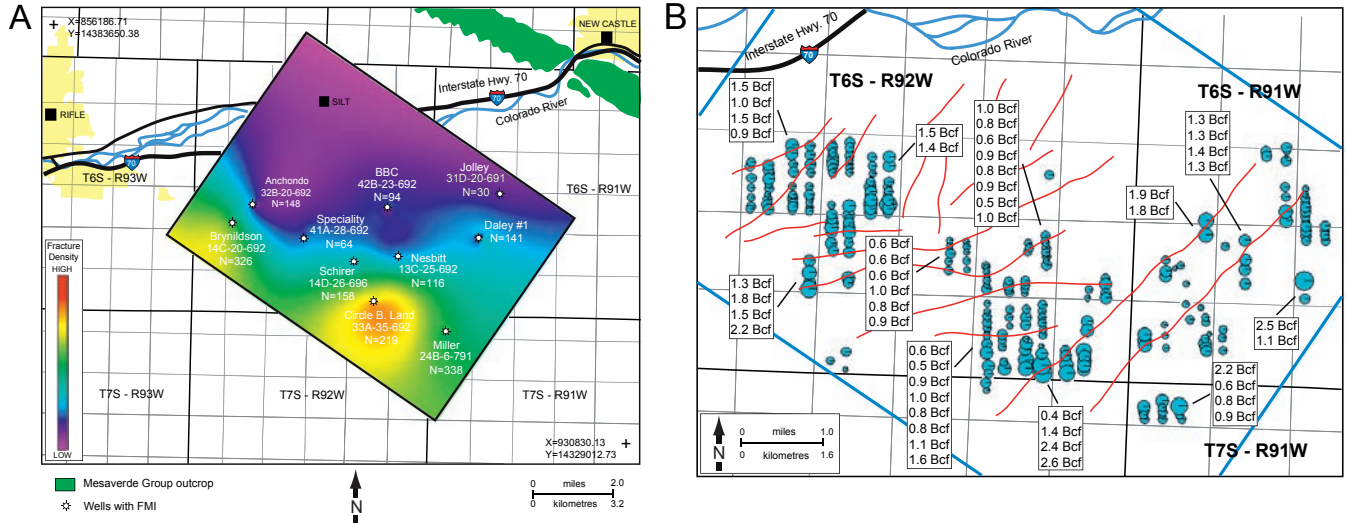


Fig. 7. (a) Fracture-intensity map for the Williams Fork Formation. (b) Map of the number of fractures per well in the study area (Price Coal–Rollins Sandstone Member).

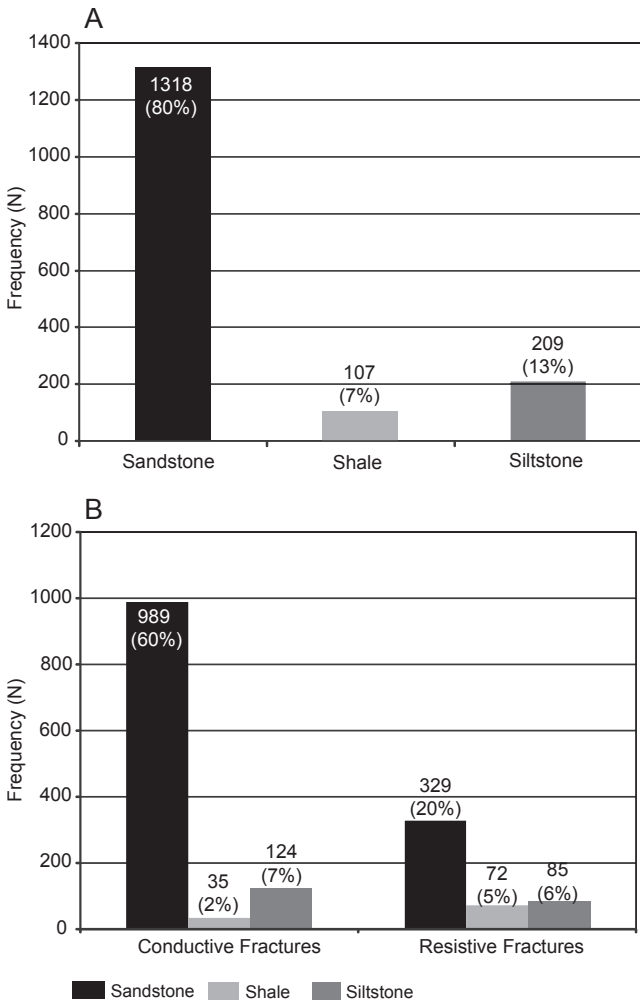


Fig. 8. Histograms of fracture frequency with respect to lithology. (a) Percentages of fractures by lithology (sandstone, siltstone and shales). More than 90% of natural fractures occur in sandstones and siltstones. (b) Percentages of fractures by fracture type and lithology. Three-quarters of natural fractures in sandstones are conductive fractures.

this interval in comparison with the number of conductive fractures in fluvial and marine intervals.

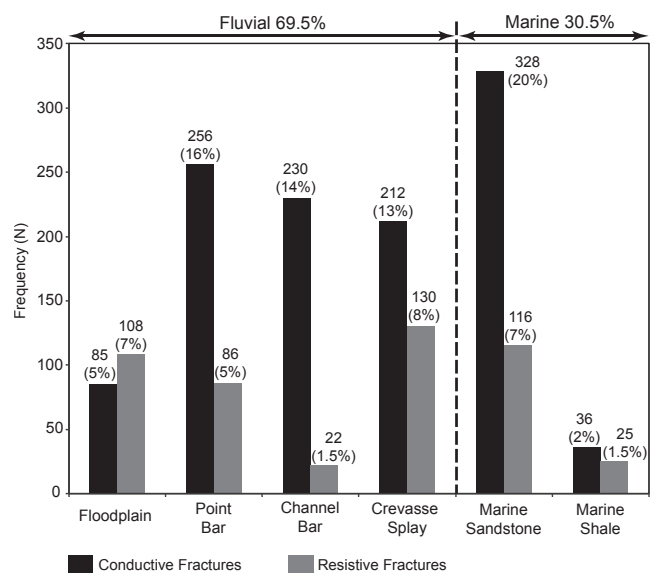
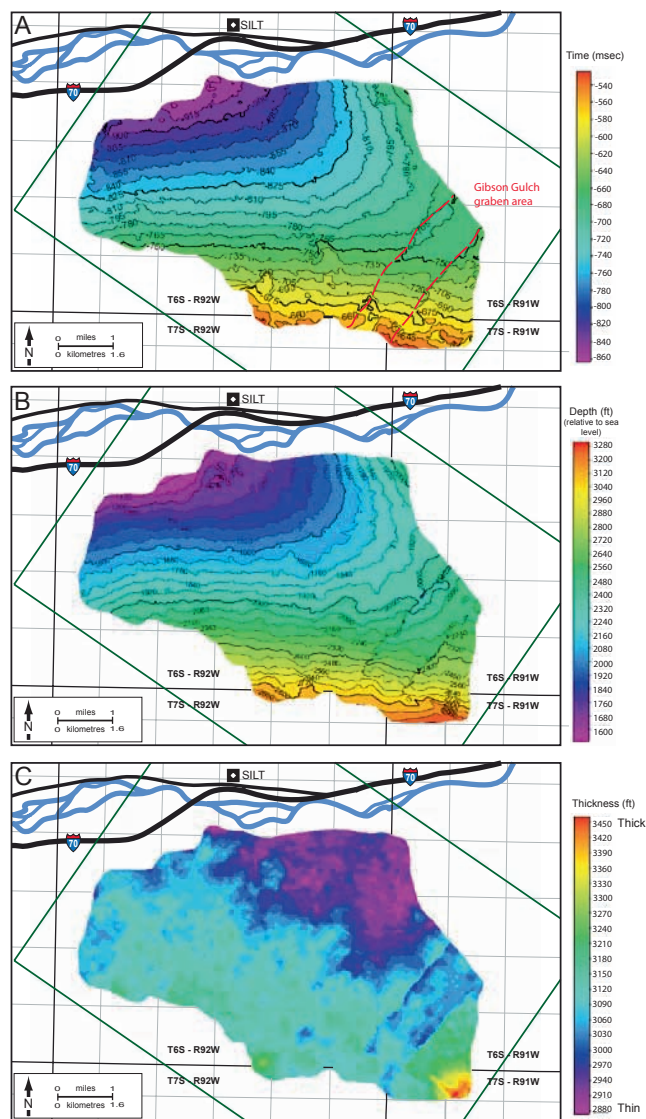


Fig. 9. Histogram of fracture frequency with respect to architectural elements, fracture type and depositional setting; 69.5% of natural fractures were observed in fluvial deposits, whereas 30.5% were observed in marine deposits.

**Seismic characteristics of stratigraphic units**

Unconformities at the top and the base of the Ohio Creek Member are evident from onlapping reflections in the seismic data. The top and the base of the Ohio Creek Member are both expressed by positive amplitude (peak); however, they are different in reflection strength. The unconformity at the top of the Ohio Creek Member (top Mesaverde Group) is expressed by moderate–high positive amplitude (peak) in comparison with the unconformity at the base of the Ohio Creek Member, which is fair–moderate in strength. This difference may indicate different acoustic impedance contrasts between the beds above and below the unconformities. In terms of reflection continuity, the top Ohio Creek horizon exhibits moderate reflection continuity, and the base Ohio Creek horizon exhibits moderate reflection continuity that is problematic to interpret in some areas. Manual interpretation using formation tops was conducted in such areas. Internal reflection configuration of the



**Fig. 10.** (a) Time–structure contour map, (b) depth–structure contour map and (c) isopach map of the Williams Fork Formation interval interpreted from 3D seismic data. The Gibson Gulch Graben area is present on structure contour maps both in time and depth. The isopach map shows a thickness variation of this interval. The irregular shape is due to an uninterpreted area where data are either poor or not available.

Ohio Creek Member is expressed by parallel–subparallel reflections that have variable reflection strength and continuity (Fig. 5). The reflection configuration variability probably reflects the types of deposits that have been interpreted as low-stand braided-fluvial rivers (Patterson *et al.* 2003). The Ohio Creek Member has a maximum thickness of 621 ft (189 m), an average thickness of 488 ft (149 m) and thins to the SE part of the study area.

The top of the Williams Fork Formation is expressed as positive amplitude (peak) that has fair–moderate amplitude strength and moderate continuity. Reflections are especially interrupted in the Gibson Gulch Graben area (Figs 5 and 10) because of the structural displacement caused by the graben. Reflector configuration of the Williams Fork Formation varies with depth and depositional environment (Fig. 5). Distinct differences in reflection configuration exist between the undifferentiated middle and upper Williams Fork Formations that were deposited in alluvial-plain and fluvial settings, and the lower

Williams Fork Formation that is characterized by lower-coastal plain and marine environments (Fig. 5). In the study area, the Williams Fork Formation has a maximum thickness of 3460 ft (1055 m), an average thickness of 3067 ft (935 m) and thins toward the Grand Hogback monocline.

The ‘undifferentiated’ middle and upper Williams Fork Formation is dominated by fluvial deposits that include sandstones, siltstones and shale. The top of the upper Williams Fork Formation has a moderately continuous positive amplitude (peak) that has fair–moderate amplitude strength. The base of the upper Williams Fork Formation has low continuity and a low negative amplitude (trough) that is difficult to interpret in some areas (Fig. 5). The most distinct feature within this interval is Price Coal, which is a thin coal 1–3 ft (0.3–0.9 m) in thickness. The Price Coal is an important seismic marker across the study area that has a highly continuous negative amplitude (trough) and a high reflection amplitude strength (Fig. 5). Cole & Cumella (2005) suggested that the Price Coal reflector can be confidently correlated from the east Parachute Field through the Mamm Creek Field. Price Coal reflections are displaced in the Gibson Gulch Graben area by tens of feet caused by the graben. Reflection configuration of the ‘undifferentiated’ middle and upper Williams Fork Formation is similar to that of the Ohio Creek Member (Fig. 5), and includes parallel–subparallel reflections, reflector offset, poor amplitude coherency and dimming of amplitudes (Fig. 5). The distinction between the middle and upper Williams Fork Formation is difficult to establish on the basis of seismic character alone because a similar lithology exists across the boundary, and therefore the change in acoustic impedance is low. The entire ‘undifferentiated’ interval of the middle and upper Williams Fork Formation has a maximum thickness of 2100 ft (640 m) and an average thickness of 1813 ft (552 m) in the study area.

Within the lower Williams Fork Formation, the top of the middle Sandstone and the Cameo-Wheeler coal zone of the Bowie Shale Member can be picked and tracked throughout seismic data; however, the South Canyon coal zone, the upper Sandstone (Bowie Shale Member) and the Coal-Ridge coal zone (Paonia Shale Member) are not resolved. Although these intervals are expressed in seismic data, interpretation is complex. The lower Williams Fork Formation in the study area has a maximum thickness of 1491 ft (454.5 m), an average thickness of 1254 ft (382 m) and thins to the NE towards the Grand Hogback. The middle Sandstone has moderate–high negative amplitude (trough) and moderate–good continuity. The presence of an unconformity surface (sequence boundary) at the top of this marine unit is evident from onlapping seismic reflections, which suggests that the South Canyon coal zone overlies this marine unit unconformably. The middle Sandstone has a maximum thickness of 395 ft (120 m), average thickness of 170 ft (51 m) and increases in thickness to the east of the study area. Onlapping reflections at the top and the base of the Cameo-Wheeler coal zone suggest that it unconformably overlies the Rollins Sandstone Member and is unconformably overlain by strata above (Fig. 5) (Patterson *et al.* 2003). The top of this interval has low–moderate positive amplitude (peak) and is moderately continuous across the study area. In terms of interval reflection configuration, although the whole interval is mostly expressed by a negative amplitude (trough), positive amplitudes are still present and interrupt negative amplitudes, suggesting that there is a change in impedance within the interval. The entire interval has a maximum thickness of 416 ft (127 m) and an average thickness of 233 ft (71 m). The Cameo-Wheeler coal zone thins to the NE part of the study area. The top of the Rollins Sandstone Member has moderate–high positive amplitude (peak) with moderately continuous reflection continuity.

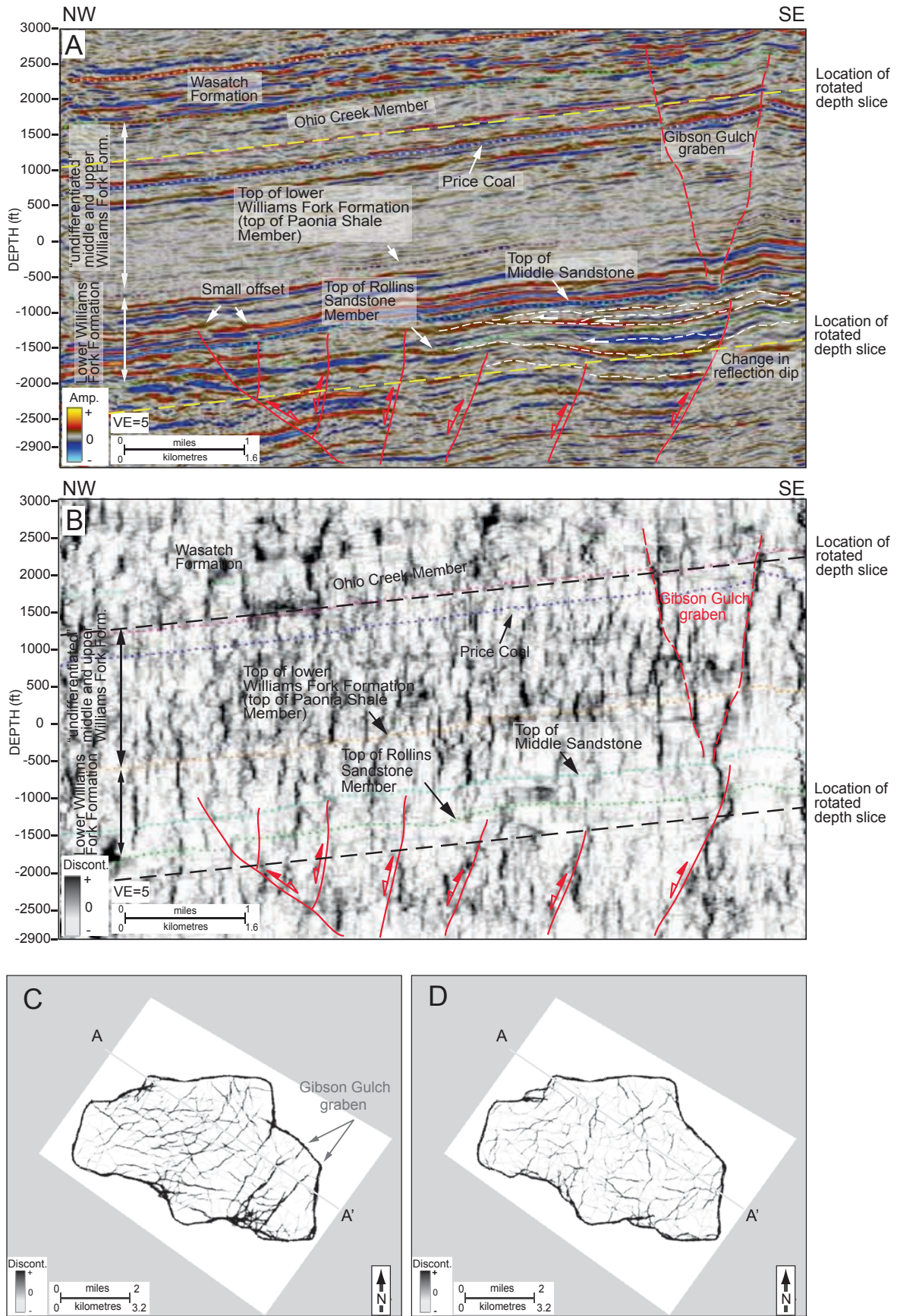


**Fig. 11.** Seismic section (cross-line 177) through (a) the seismic amplitude and (b) the ant-track attribute volumes with interpreted thrust and normal faults. Rotated depth slices through the ant-track attribute volume showing discontinuities in (c) a stratigraphically higher interval and (d) a stratigraphically lower interval of the Mesaverde Group (vertical locations of rotated depth slices are shown in seismic sections in a and b). The location of seismic section A–A' (cross-line 177) is shown in rotated depth slices in (c) and (d).

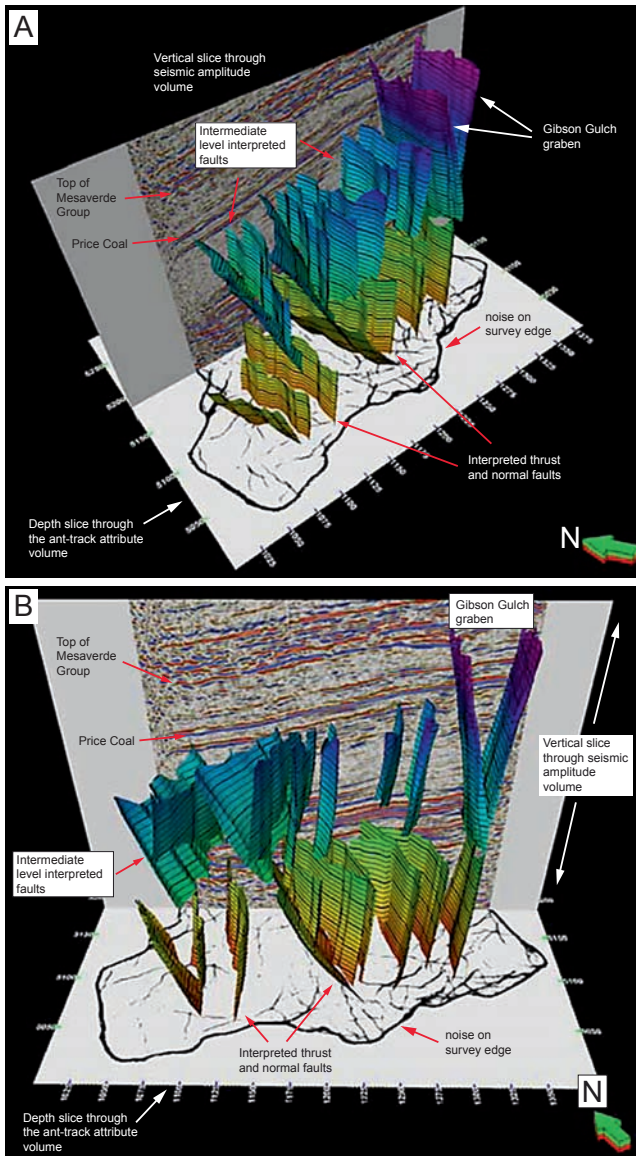


**Fig. 12.** Three-dimensional perspective views of interpreted basement-involved thrust and normal faults, intermediate-level interpreted faults and the Gibson Gulch Graben area.

### 3D seismic interpretation of faults

The type, distribution and orientation of faults vary stratigraphically. Below the middle Sandstone, small thrust and normal faults are interpreted based on seismic reflection dip (rotated fault blocks), which becomes horizontal compared to regional structural dip (Fig. 11a). The small thrust faults terminate up-section in the Rollins Sandstone Member, Cameo-Wheeler coal zone and middle Sandstone (Fig. 11). The number of small thrust faults is subjective; however, two key thrust faults are interpreted. The seismic amplitude and ant-track attribute volume show NNW-, east-west- and NE-SW-trending discontinuities, with the NNW-trend of the deep thrust and normal faults being dominant (Figs 11c, d and 12). The thrust and normal faults can be traced downwards to the Mancos Shale in the time volume, but it is difficult to relate these thrusts to a basement fault or a detachment surface owing to the limited extent of seismic data.

In the study area, the lack of observable slip on thrust and normal faults can be explained by positive inversion. (Coward 1994, p. 289) describes the term 'inversion' as 'regions which have experienced a reversal in uplift or subsidence that is, areas which

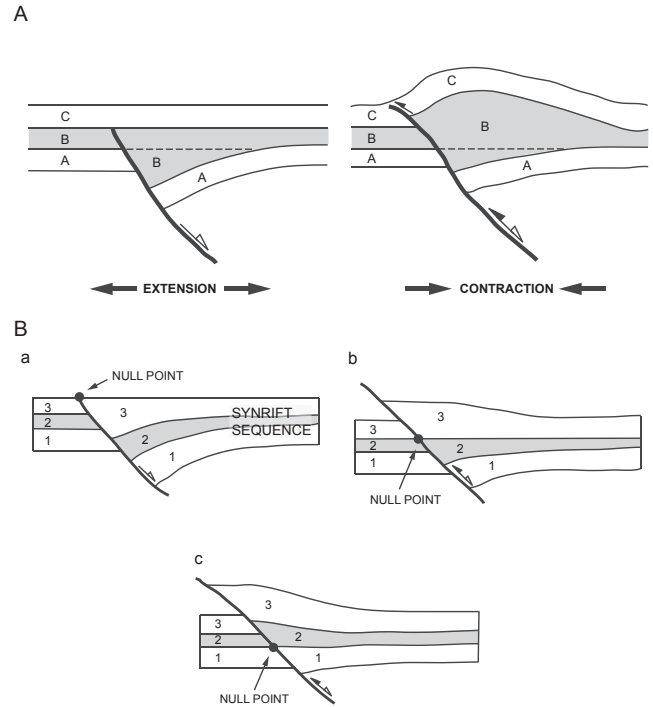


**Fig. 13.** (a) Schematic diagram of a classical positive inversion structure. Stratigraphic intervals include pre-rift A, syn-rift B and post-rift C. (b) Sequential diagrams to show the compressional inversion of an extensional fault. The null point shifts down the syn-rift interval with increased contractional inversion (modified from Williams *et al.* 1989).

have changed from being regions of subsidence to regions of uplift, or vice versa'. When structural inversion occurs, the change from subsidence to uplift is considered positive inversion, and the change from uplift to subsidence is considered negative inversion (Harding 1985; Williams *et al.* 1989; Coward 1994). Positive inversion results in each fault retaining displacement caused by extension and an anticline growth in the upper portion of faults caused by contraction (Fig. 13) (Williams *et al.* 1989). During the contractional fault movement, the top and base sequence markers move upwards, retaining their positions and either exhibit no displacement or appear unfaulted (Fig. 13) (Williams *et al.* 1989). This point is defined as the null point, which shifts downwards during the progressive movement of an extensional synrift sequence caused by contraction (Fig. 13) (Williams *et al.* 1989). Therefore, contraction following extension has caused individual faults to retain net extension at depth, which explains the lack of observable slip on seismic reflections and produces a null point at the Mancos Shale level (Fig. 14) (Williams *et al.* 1989).

Basement features and their relationship to shallower structures have long been discussed in the Piceance Basin. Particularly, Hoak & Klawitter (1997) and Kuuskraa *et al.* (1997b) suggested basement-controlled thrusting that causes faulting and fracturing in the Mesaverde Group. In the study area, vertical sections through the ant-track attribute volume indicate discontinuities at tip lines of the thrust and normal faults (Fig. 11b). A small amount of offset on shallow reflections and high ant-track attribute values appears to continue up-section from the tip line of thrust and normal faults (Fig. 11b). This relationship may have been complicated by overpressuring, which also plays a role in fracture occurrence. As produced in laboratory experiments, faults create perturbations in the regional stress field at their terminations; thus, a fault tip creates zones of increased tension and compression (Logan *et al.* 1979; Kuuskraa *et al.* 1997b). As a result, fracture density and permeability can be expected to be influenced by thrusting and faulting.

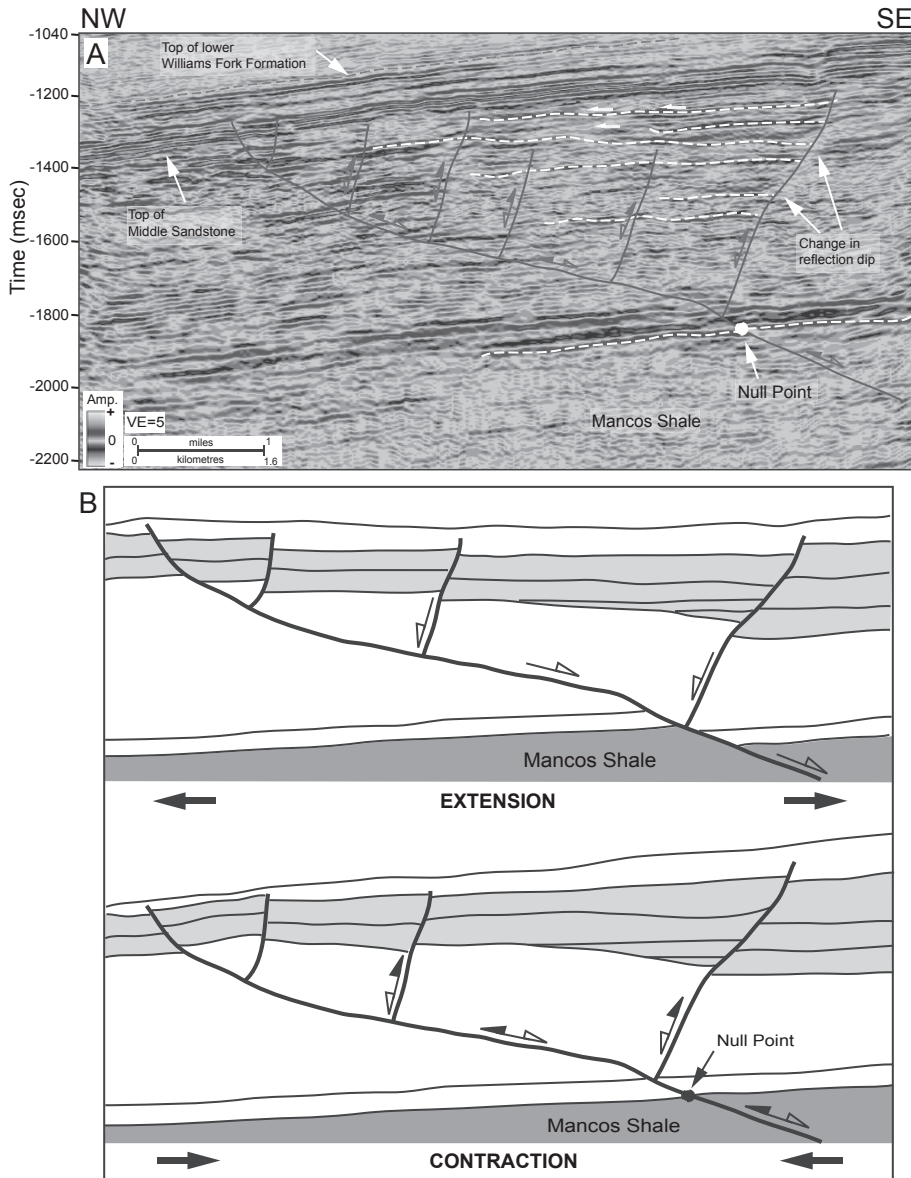


**Fig. 14.** (a) Seismic section (cross-line 177) through the seismic data in time. The interpreted thrust fault can be traced back to the Mancos Shale level. The lack of observable slip on the faults is explained by a null point as a consequence of positive inversion, which resulted from a change from extension to contraction in the study area. (b) Inversion-type model to explain the lack of observable slip on faults. The location of the section (cross-line 177) is shown in Figure 2.

In intermediate levels in the study area, reflectors exhibit amplitude dimming, poor amplitude coherency and reflector offset. Depth slices through the ant-track attribute volume indicate east-west- and NNE-trending discontinuities. It appears that east-west-trending discontinuities become NNE-trending closer to the Grand Hogback. The NE-trending Gibson Gulch Graben is also evident (Figs 11 and 12). In shallow levels, east-west-trending faults become dominant (Fig. 11c). Within the upper and middle Williams Fork Formation, the subsurface structure is complicated owing to fracturing caused by overpressuring, and faulting and fracturing related to basement structures. The ant-track attribute anomalies may indicate higher fracture intensity and faulting associated with thrust faults deeper in the Cameo-Wheeler coal zone and Rollins Sandstone Member levels. It is very likely that thrust and normal faults may penetrate through this section and terminate as a broad area of fracture clusters.

### 3D seismic-based fracture intensity and distribution

Seismic attribute and fracture relationships were examined for eight different zones throughout the seismic survey area. Additional

ant-track volumes were generated to analyse relationships between fracture intensity and seismic attributes. The ant-track workflow was adopted again to generate ant-track attribute volumes, except that structural smoothing was omitted because, for fracture analysis, small-scale discontinuities can be significant and structural smoothing reduces these features. Structural smoothing when applied tends to increase the continuity of the seismic reflectors; therefore, it may cause the loss of events that may be related to fractures. Ant-track attributes were extracted along the wellbores and quantitatively and visually compared to fracture intensity (Fig. 15). In order to obtain an attribute volume that has the most reasonable relationship with the fracture intensity, 20 different ant-track attribute volumes (20 different realizations) were generated. The correlation has been performed between the seismic attribute values and fracture-intensity log values for the cells crossing the wellbore. The cross-plotting of these quantities shows a reasonable correlation. The relationships were examined for mechanical intervals and exhibit correlation coefficients that range from 0.55 to 0.75 (Figs 15 & 16).

Higher  $t^*$  values can indicate higher fracture intensity, thicker fractured stratigraphic units or a combination of both;

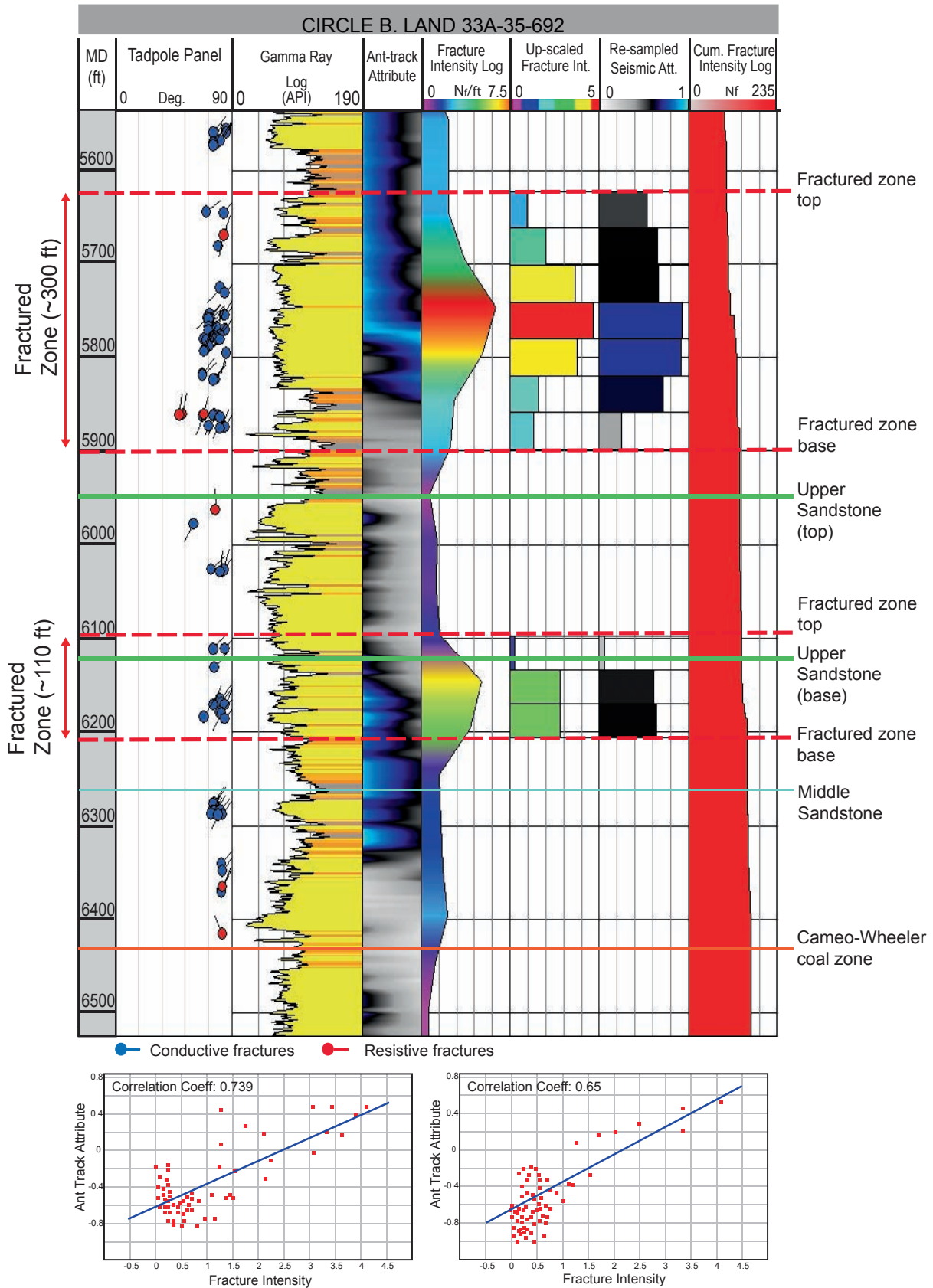


**Fig. 15.** Well Circle B. Land (see Fig. 7 for the location.). Data show a tadpole plot of natural fractures, gamma-ray log (API), ant-track attribute extracted along the wellbore, fracture-intensity log, up-scaled fracture-intensity log and resampled ant-track attribute for two zones. The cumulative-intensity log is displayed on the last track. Ant-track attribute extraction along the wellbore was done by using -50 to 50 as the start and end distance. Two cross-plots (bottom) show the correlation between {logged/up-scaled} fracture intensity and the ant-track attribute for the two zones shown; the correlation coefficients support the visual evidence for a relationship between the two quantities. The cross-plots shown include the data at all well locations where the upscaling was done.

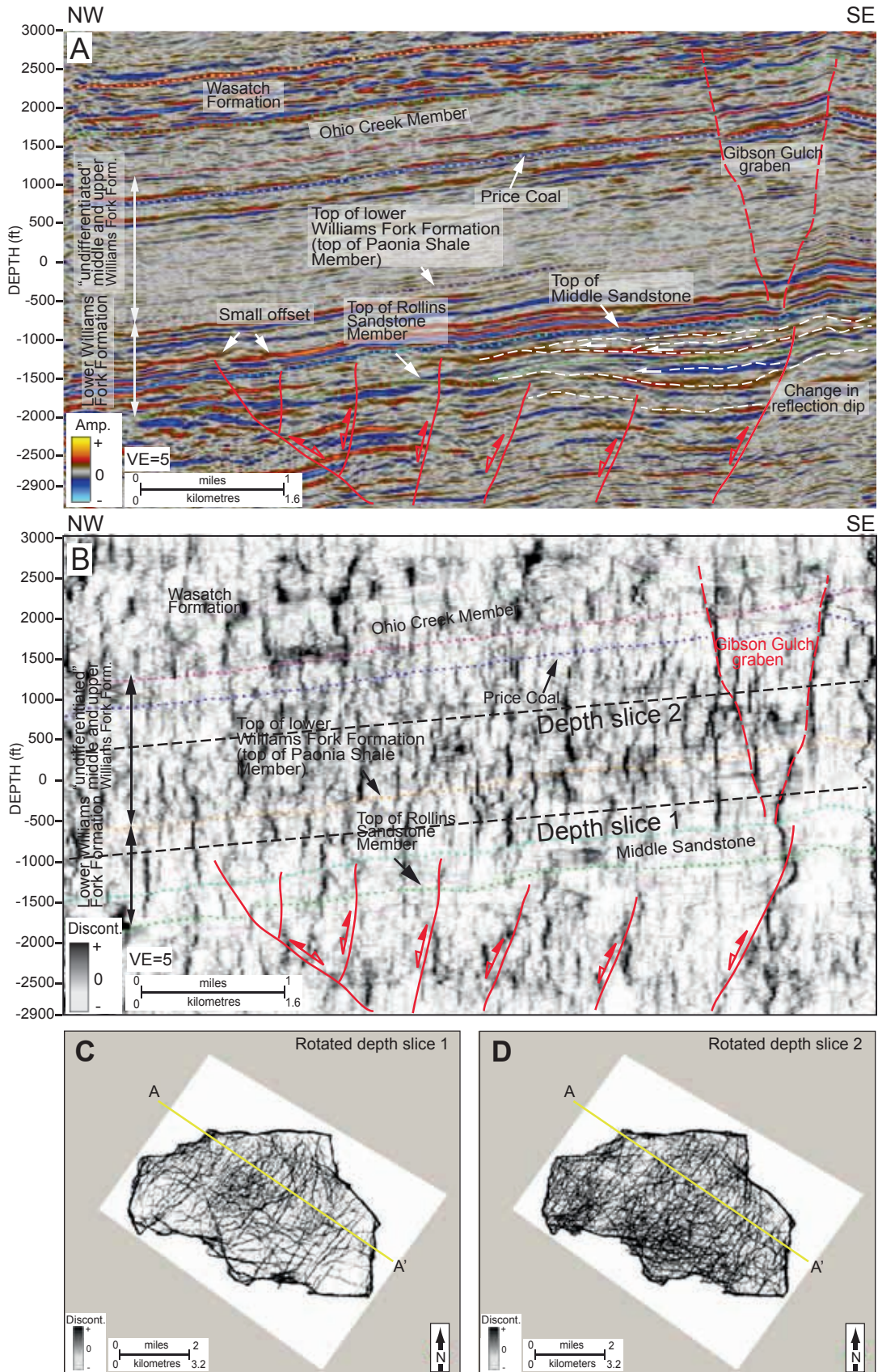


**Fig. 16.** Seismic section (cross-line 177) through (a) the seismic amplitude and (b) the ant-track attribute volumes with interpreted thrust and normal faults. Ant-track attributes were extracted along the wellbores, and quantitatively and visually compared to fracture intensity. The relationships were examined for eight stratigraphic intervals and exhibit correlation coefficients that range from 0.55 to 0.75; in general, a positive relationship exists between the ant-track attribute and the fracture intensity based on borehole images. Rotated depth slices show ant-track attributes for two stratigraphic levels (locations are shown in b) as an indicator of potential fractured areas.

Fault and fracture distribution within tight-gas sands

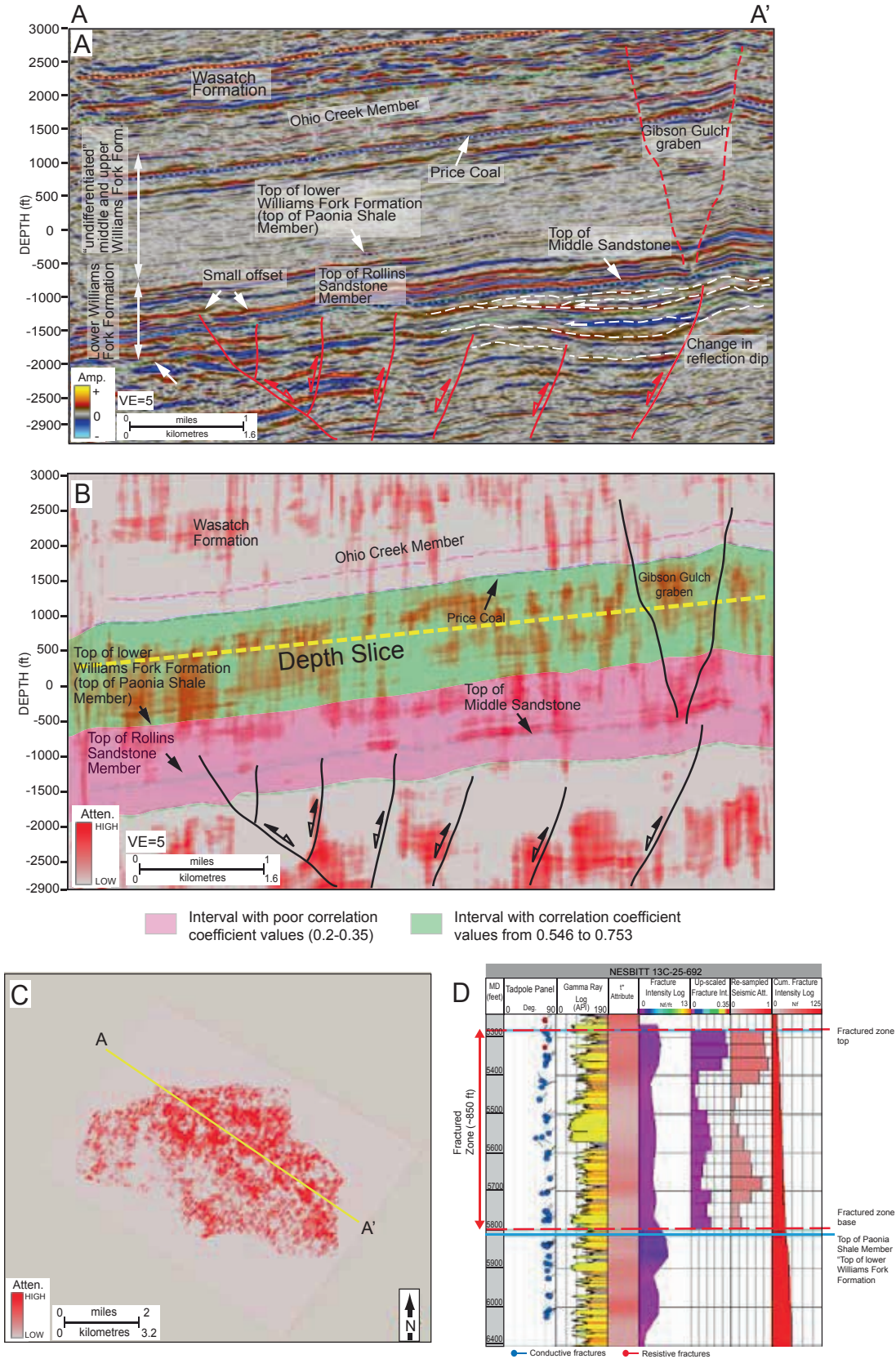


**Fig. 17.** Seismic section (cross-line 177) through (a) the seismic amplitude and (b) the  $t^*$  attenuation attribute volumes with interpreted thrust and normal faults. The  $t^*$  attributes were extracted along the wellbores, and quantitatively and visually compared to fracture intensity. The relationships were examined for eight stratigraphic intervals and exhibit correlation coefficients that range from 0.55 to 0.75. In the middle and upper Williams Fork Formation (shown in green in b) interval, reasonable results were obtained; however, with greater depth in the lower Williams Fork Formation (shown in red in b), the relationship between fracture intensity and  $t^*$  attributes has a lower correlation coefficient that ranges from 0.2 to 0.35. (c) Rotated depth slice through the  $t^*$  attenuation attribute volume (see b for the location). Red areas indicate high  $t^*$  values as an indicator of potential fractured areas. (d) Nesbitt well log data show a tadpole panel of natural fractures, gamma-ray log (API) and  $t^*$  attenuation attributes extracted along the wellbore, fracture-intensity log, up-scaled fracture-intensity log and resampled  $t^*$  attenuation attributes for a 850 ft- (259-m-) thick zone.

however, frequency attenuation can also be caused by layering, interference and multiples (Najmuddin 2003). In order to examine the relationship between  $t^*$  attributes and fracture-intensity logs, different  $t^*$  attenuation attribute cubes were generated and cross-plotted with up-scaled fracture-intensity logs for eight mechanical zones. The cross-plotting of these two quantities shows correlation coefficients that range from approximately 0.55 to 0.75. In the middle and upper Williams Fork Formation interval, reasonable correlations were obtained; however, at greater depth in the lower Williams Fork Formation, the relationship between fracture intensity and  $t^*$  attributes has a lower correlation coefficient that ranges from 0.2 to 0.35 (Fig. 17). These lower correlation coefficients in the lower portion of the Williams Fork Formation are due to attenuation of frequencies by depth. Owing to attenuation, frequency content decreases. As the frequency content changes, parameters such as high and low frequency and the length of the extraction window (number of cycles) that are acceptable for shallow intervals will no longer be applicable for the lower Williams Fork Formation (Fig. 17). This lower portion should be evaluated independently by applying different high- and low-frequency values, and different extraction window length due to changes in the amplitude spectrum of the frequencies.

## DISCUSSION

Conductive fractures of the Mesaverde Group have a dominant strike orientation of N45°W, and the strike orientation of resistive fractures ranges from N40°W to N80°W. A NNE strike orientation was also observed for a small number of resistive fractures. The cause of scatter for resistive-fracture strike orientation is unclear; however, it could be associated with changing stress orientation through time. The natural fracture orientation is believed to be primarily controlled by the horizontal compressive stress orientation associated with the Laramide Orogeny (Lorenz & Finley 1991). Sixty per cent of natural fractures terminate against lithological boundaries, and 90% of natural fractures occur in sandstones and siltstones. This is consistent with interpretations of Lorenz & Finley (1989, 1991) and Northrop & Frohne (1990). Based on architectural-element logs, 70% of natural fractures occur in fluvial deposits and only 30% occur in marine deposits. The fluvial sandstone reservoirs of the Mesaverde Group differ significantly from marine sandstone reservoirs. Fluvial reservoirs are lenticular in shape, are commonly discontinuous, and contain internal lithological heterogeneities in terms of grain size, sedimentary structure and permeability. Conversely, marine sandstone reservoirs are more laterally continuous and have more uniform internal characteristics, reflecting few internal discontinuities. Lorenz & Finley (1989) indicated that the distribution of fractures appears to be associated with depositional environment and associated lithological variability (Lorenz & Finley 1989; Baytok 2010). In the study area, this observation is obscured by the limited well depths penetrating into deeper marine units, and fracture occurrences appear to show no apparent relationship regarding the depositional environment (fluvial v. marine). Interpretations of the origin of fracture formation are varied. However, a common view is that fracture formation is likely to be associated with high pore pressures related to burial, periods of regional uplift and erosion, local faulting and folding, and regional stresses (Pitman & Sprunt 1986; Lorenz & Finley 1989; Cumella & Scheevel 2008).

*In situ* stress analysis based on induced-tensile fractures and borehole breakouts reveals a NNW orientation of present-day maximum horizontal compressive stress, which is consistent with the orientation of conductive fractures in the area. Of

interest, *in situ* stress analysis also indicates approximately a 20° rotation in the stress field stratigraphically. Such information is useful in reservoir-development planning and reservoir-modelling predictions. Fracture strike and *in situ* stress orientations derived from borehole-image logs are consistent with previous interpretations (Verbeek & Grout 1984; Pitman & Sprunt 1986; Lorenz & Finley 1989, 1991; Grout & Verbeek 1992; Hoak & Klawitter 1997; Nelson 2003).

Fracture intensity based on borehole-image logs is greater in the southern and western portions of the study area (Fig. 7a). This is concluded based on fracture-intensity maps and seismic attribute depth slices. Wells with gas production rates that are greater than 2BCF are present in the area where fracture intensity is greatest. Even though some wells in the area are stimulated by hydraulic fracturing, well estimated ultimate recovery (EUR) rates show a consistent relationship between natural-fracture intensity and productivity.

Relationships between the ant-track and  $t^*$  attenuation attributes and fracture intensity were examined for eight stratigraphic intervals and exhibit correlation coefficients that range from 0.55 to 0.75; in general, a moderate and positive relationship exists. The  $t^*$  attenuation attribute, however, gives lower correlation coefficient values of 0.2–0.35 in the lower Williams Fork Formation. This is due to the different frequency content of the seismic data and is explained by the attenuation of frequencies with increasing depth. Vertical ant-track-attribute profiles and rotated depth slices of ant-track attributes for two stratigraphic levels show the distributions of potentially fractured areas in the Mesaverde Group (Fig. 16). For the  $t^*$  attributes, the difference in correlation coefficient between the middle and upper Williams Fork formations v. lower Williams Fork Formation (Fig. 17) is believed to be caused, in part, by the different seismic properties associated with these stratigraphic zones. In addition, because frequency characteristics of seismic data change with depth and frequencies are attenuated, differences associated with the seismic attribute can exist that are not related to fracture intensity.

This study reveals the existence of thrust and normal faults in the study area based on 3D seismic interpretation (Fig. 12) (Baytok 2010). The thrust faults can be traced deep into the Mancos Shale; however, seismic data coverage is unable to confirm the existence of a possible Mancos-level detachment and the relationship of the thrust faults to deeper basement faults. Hoak & Klawitter (1997) emphasized the importance of a Mancos-level detachment in the central and eastern basin based on detailed aeromagnetic data calibrated with seismic data. The interpreted thrust faults might be related to a basement-involved wedge whose surface expression is the Grand Hogback monocline and NNW-trending intrabasin folds of the Wolf Creek and Divide Creek anticlines south of the study area (Grout & Verbeek 1992). Normal faults that are related to thrust faulting are also interpreted in the study area. Thrust faults and normal faults exhibit minimal to small-scale offset in the Rollins Sandstone Member, Cameo-Wheeler coal zone and middle Sandstone. The change in offset along the faults is explained by positive inversion that resulted from fault reactivation.

## CONCLUSIONS

The Piceance Basin of NW Colorado is one of several Rocky Mountain basins that produce from fractured tight-gas sandstones of the Mesaverde Group. The interpretation of borehole-image logs indicates that conductive fractures occur in sandstones twice as frequently as resistive fractures. Fracture-intensity maps and seismic attributes show a variable distribution of fractures with higher fracture intensity on the southern and western portions of the study area. The orientation of present-day maximum horizontal

compressive stress ( $S_{H_{max}}$ ) is NNW in the area, based on borehole breakouts and induced-tensile fractures. This orientation is consistent with the strike orientation of conductive fractures of N45°W. The dip azimuth of induced-tensile fractures and borehole breakouts shows an approximately 20° clockwise rotation in the orientation of  $S_{H_{max}}$  and a 20° sudden shift at 7200 ft (2195 m) in the Rollins Sandstone Member. It is impossible to determine whether there is a shift back below the depth of 7200 ft (2195 m) in the Rollins Sandstone Member due to limited well depths. Fracture analysis indicates that natural fractures (more than 90%) occur in sandstones and siltstones, and terminate against lithological boundaries. Only a few low-angle resistive fractures occur in shale. Seventy per cent of fractures occur in fluvial deposits v. 30% in marine deposits. Based on the data, fracture occurrences show no apparent relationship regarding the depositional environment (fluvial v. marine) and depth. Only one well penetrates deep enough to have fracture data in the Cozzette and Corcoran marine sandstone intervals, and the limited well depths cause a difficulty in the interpretation of the depositional environment control on the distribution of natural fractures. The magnitude of fracture intensity in point bars, channel bars and crevasse splays does not differ significantly; however, resistive fractures occur less often in channel bars (middle and upper Williams Fork formations) than in point bars and crevasse splays (lower Williams Fork Formation). Seismic attribute analysis reveals correlation coefficients of 0.55–0.75 for both ant-track and  $t^*$  attenuation attributes between seismic attributes and fracture intensity. Lower correlation coefficient values of 0.2–0.35 are obtained for  $t^*$  attenuation attributes alone in the lowermost lower Williams Fork Formation.

In the study area, each stratigraphic surface and interval differs in reflection continuity, reflection strength and reflection configuration based on their structural and stratigraphic (depositional) characteristics. For example, the seismic expression of the ‘undifferentiated’ middle and upper Williams Fork Formation (braided-fluvial deposits) exhibits poor amplitude coherency, amplitude dimming and parallel–subparallel reflections. The ant-tracking workflow, which was used to generate an enhanced fault volume, helps to interpret the type, distribution and orientation of faults in collaboration with the seismic amplitude and curvature volumes. The results reveal the presence of small thrust and normal faults deeper in the stratigraphic interval. Dip changes in reflections suggest a rotation of the blocks as a consequence of thrusting, and reflections become almost horizontal and differ from the regional structural dip. The lack of observable slip on the faults at Mancos Shale level is explained by positive inversion that caused the reactivation of faults, and caused markers to move upwards and retain their positions, exhibiting no displacement or appearing unfaulted. Depth slices through the ant-track attribute volume in the lower part of the stratigraphic interval that was analysed show NNW-, east–west- and NE–SW-trending discontinuities; however, the NNW strike orientation of thrust and normal faults appears to be dominant. The amplitude dimming, poor amplitude coherency and reflector offset in the ‘undifferentiated’ middle and upper Williams Fork Formation interval results in a highly complex ant-track attribute expression of discontinuities that makes interpretation of individual faults difficult. Depth slices through the ant-track attribute volume for the middle and upper Williams Fork formations indicate that the east–west- and NNE-trending discontinuities are more prevalent towards the Grand Hogback monocline. The Price Coal, Ohio Creek Member and stratigraphically shallower intervals exhibit only east–west-trending discontinuities.

Financial support was provided by the Reservoir Characterization and Modeling Laboratory (RCML) at the University of Colorado at Boulder through a grant from the Research Partnership to Secure Energy for America (RPSEA). We thank B. Trudgill and G. Dorn for their input and valuable discussions. We acknowledge Bill Barrett Corporation and

EnCana Oil and Gas (USA) Inc. for access to cores, and Bill Barrett Corporation for providing well-log data. We thank Schlumberger for data and support with borehole-image-log analysis and interpretation.

## REFERENCES

- Baytok, S. 2010. Seismic investigation and attribute analysis of faults and fractures within a tight-gas sandstone reservoir: Williams Fork Formation, Mamm Creek Field, Piceance Basin, Colorado. MS thesis, University of Colorado, Boulder, CO.
- Carmichael, R.S. 1989. *Practical Handbook of Physical Properties of Rocks and Minerals*. University of Iowa Department of Geology, Iowa city. CRC Press, Boca Raton, FL.
- Carroll, C.J., Robeck, E., Hunt, G. & Koontz, W. 2004. Structural implications of underground coal mining in the Mesaverde Group in the Somerset coal field, Delta and Gunnison counties, Colorado. In: Nelson, E.P. & Erslev, E.A. (eds) *Field Trips in the Southern Rocky Mountains, USA*. Geological Society America, Field Guides, **5**, 41–58.
- Cole, R.D. & Cumella, S.P. 2005. Sand-body architecture in the lower Williams Fork Formation (Upper Cretaceous), Coal Canyon, Colorado, with comparison to the Piceance Basin subsurface; Cretaceous sand body geometries in the Piceance Basin area of northwest Colorado. *The Mountain Geologist*, **42**, 85–107.
- Collins, B.A. 1976. Coal deposits of the Carbonale, Grand Hogback, and southern Danforth Hills coal fields, eastern Piceance basin, Colorado. *Quarterly of the Colorado School of Mines*, **71**, (1).
- Coward, M. 1994. Inversion tectonics. In: Hancock, P.L. (ed.) *Continental Deformation*. Pergamon Press, New York, 289–304.
- Cumella, S.P. & Ostby, D.B. 2003. Geology of the basin-centered gas accumulation, Piceance Basin, Colorado. In: Peterson, K.M., Olson, T.M. & Anderson, D.S. (eds) *Piceance Basin 2003 Guidebook*. Rocky Mountain Association of Geologists, Denver, CO, 171–193.
- Cumella, S.P. & J. Scheevel, J. 2008. The influence of stratigraphy and rock mechanics on Mesaverde gas distribution, Piceance Basin, Colorado. In: Cumella, S.P., Shanley, K.W. & Camp, W.K. (eds) *Understanding, Exploring, and Developing Tight-gas Sands – 2005 Vail Hedberg Conference*. American Association of Petroleum Geologists, Hedberg Series, **3**, 137–155.
- Gibson, R.L., Theophanis, S. & Toksoz, M.N. 2000. Physical and numerical modeling of tuning and diffraction in azimuthally anisotropic media. *Geophysics*, **65**, 1613–1621.
- Grout, M.A., Abrams, G.A., Tang, R.L., Hainsworth, T.J. & Verbeek, E.R. 1991. Late Laramide thrust related and evaporite-domed anticlines in the southern Piceance Basin, northeastern Colorado Plateau. *American Association of Petroleum Geologists Bulletin*, **75**, 205–218.
- Grout, M.A. & Verbeek, E.R. 1992. *Fracture History of the Divide Creek and Wolf Creek Anticlines and its Relation to Laramide Basin-margin Tectonism, Southern Piceance Basin, Northwestern Colorado (16 Structural Geology; 29A Economic Geology, Geology of Energy Sources No. B 1787-Z)*. United States Geological Survey, Reston, VA.
- Harding, T.P. 1985. Seismic characteristics and identification of negative flower structures, positive flower structures, and positive structural inversion. *American Association of Petroleum Geologists Bulletin*, **69**, 582–600.
- Haugen, G.U. & Schoenberg, M.A. 2000. The echo of a fault or fracture. *Geophysics*, **65**, 176–189.
- Hettinger, R.D. & Kirschbaum, M.A. 2002. *Stratigraphy of the Upper Cretaceous Mancos Shale (Upper Part) and Mesaverde Group in the Southern Part of the Uinta and Piceance Basins, Utah and Colorado*. United States Geological Survey, Geologic Investigations Series, **1-2764**.
- Hettinger, R.D. & Kirschbaum, M.A. 2003. *Stratigraphy of the Upper Cretaceous Mancos Shale (Upper Part) and Mesaverde Group in the Southern Part of the Uinta and Piceance Basins, Utah and Colorado. Petroleum Systems and Geological Assessment of Oil and Gas in the Uinta–Piceance Province, Utah and Colorado*. United States Geological Survey Uinta–Piceance Assessment Team Report, **DDS-0069-B**.
- Hoak, T.E. & Klawitter, A.L. 1997. Prediction of fractured reservoir production trends and compartmentalization using an integrated analysis of basement structures in the Piceance basin, western Colorado. In: Hoak, T.E., Klawitter, A.L. & Blomquist, P.K. (eds) *Fractured Reservoirs: Characterization and Modeling*. Rocky Mountain Association of Geologists, Denver, CO, 67–102.
- Hurley, N. 2004. Borehole Images. In: In: Asquith, G. & Krygowski, D. (eds) *Basic Well Log Analysis*. American Association of Petroleum Geologists, Methods in Exploration, **16**, 151–163.
- Johnson, R.C. 1989. *Geological History and Hydrocarbon Potential Of Late Cretaceous-Age, Low-permeability Reservoirs, Piceance Basin, Western*

- Colorado (29A *Economic Geology, Geology of Energy Sources; 06A Sedimentary Petrology; 12 Stratigraphy No. B 1787-E*). United States Geological Survey, Reston, VA.
- Johnson, R.C. & Flores, R.M. 2003. History of the Piceance Basin from latest Cretaceous through early Eocene and the characterization of lower Tertiary sandstone reservoirs. In: Peterson, K.M., Olson, T.M. & Anderson, D.S. (eds) *Piceance Basin 2003 Guidebook*. Rocky Mountain Association of Geologists, Denver, CO, 21–61.
- Johnson, R.C. & May, F. 1980. A study of the Cretaceous-Tertiary unconformity in the Piceance Basin, Colorado – The underlying Ohio Creek Formation (Upper Cretaceous) redefined as a member of the Hunter Canyon or Mesaverde Formation. *United States Geological Survey Bulletin*, **1482-B**.
- Johnson, R.C. & Roberts, S.B. 2003. The Mesaverde total petroleum system, Uinta–Piceance province, Utah and Colorado (Chapter 7). In: *Petroleum Systems and Geological Assessment of Oil And Gas in the Uinta–Piceance Province, Utah and Colorado*. United States Geological Survey, Digital Data Series, **DDS-69-B**.
- Kuuskräa, V.A. 2007. *Advanced Resources International, Inc. White Paper. Unconventional Gas Series, July, 2007*. <http://www.advres.com/pdf/Unconventional-Gas-literature.asp>
- Kuuskräa, V.A., Decker, D. & Lynn, H.B. 1997a. Optimizing technologies for detecting natural fractures in the tight sands of the Rulison Field, Piceance Basin. In: *Proceedings of the Natural Gas Conference Emerging Technologies for the Natural Gas Industry*, paper NG6-3.
- Kuuskräa, V.A., Campagna, D. & Decker, D. 1997b. Application of high fold, multi-azimuth 3-D P-wave seismic to characterize natural fractures in the Rulison field, Piceance basin. In: Coalson, E.B., Osmond, J.C. & Williams, E.T. (eds) *Innovative Applications of Petroleum Technology in the Rocky Mountain area*. Rocky Mountain Association of Geologists, Denver, CO.
- Liu, E., Crampin, S. & Hudson, J.A. 1997. Diffraction of seismic waves by cracks with application to hydraulic fracturing. *Geophysics*, **62**, 253–265.
- Logan, J.M., Friedman, M. & Stearns, M.T. 1979. Experimental folding of rocks under confining pressure: Part VI. Further studies of faulted drape folds. In: Matthews, V. (ed.) *Laramide Folding Associated with Basement Block Faulting in the Western United States*. Geological Society of America, Memoirs, **151**, 79.
- Lorenz, J.C. 1997. Heartburn in predicting natural fractures; the effects of differential fracture susceptibility in heterogeneous lithologies. In: Hoak, T.E., Klawitter, A.L. & Blomquist, P.K. (eds) *Fractured Reservoirs: Characterization and Modeling*. Rocky Mountain Association of Geologists, Denver, CO.
- Lorenz, J.C. 2003. Fracture systems in the Piceance Basin, overview and comparison with fractures in the San Juan and Green River basins. In: Peterson, K.M., Olsen, T.M. & Anderson, D.S. (eds) *Piceance Basin 2003 Guidebook*. Rocky Mountain Association of Geologists, Denver, CO, 75–94.
- Lorenz, J.C. & Finley, S.J. 1989. Differences in fracture characteristics and related production; Mesaverde Formation, northwestern Colorado. *SPE Formation Evaluation*, **4**, 11–16.
- Lorenz, J.C. & Finley, S.J. 1991. Regional fractures II: Fracturing of Mesaverde reservoirs in the Piceance basin, Colorado. *American Association of Petroleum Geologists Bulletin*, **75**, 1738–1757.
- Moos, D. & Zoback, M.D. 1990. Utilization of observations of wellbore failure to constrain the orientation and magnitude of crustal stresses: Application to continental, Deep Sea Drilling Project and Ocean Drilling Project boreholes. *Journal of Geophysical Research*, **95**, 9305–9325.
- Najmuddin, I. 2001. Detecting fracture zones in the Austin chalk using seismic P-wave data. *Bulletin of the Houston Geological Society*, **44**, 22–27.
- Najmuddin, I. 2003. *Austin Chalk fracture mapping using frequency data derived from seismic data*. PhD dissertation, Texas A&M University.
- Nelson, P.H. 2003. A review of the multiwell experiment, Williams Fork and Iles Formations, Garfield County, Colorado. In: *Petroleum Systems and Geologic Assessment of Oil and Gas in the Uinta–Piceance Province*. United States Department of the Interior Report, **DDS-0069-B**.
- Northrop, D.A. & Frohne, K. 1990. The Multiwell experiment – a field laboratory in tight gas sandstone reservoirs. *Journal of Petroleum Technology*, **42**, 772–779.
- Patterson, P.E., Kronmueller, K. & Davies, T.D. 2003. Sequence stratigraphy of the Mesaverde Group and Ohio Creek Conglomerate, northern Piceance Basin, Colorado. In: Peterson, K.M., Olson, T.M. & Anderson, D.S. (eds) *Piceance Basin 2003 Guidebook*. Rocky Mountain Association of Geologists, Denver, CO, 115–129.
- Pedersen, S.I., Randen, T., Sonneland, L. & Steen, O. 2002. Automatic fault extraction using artificial ants. In: *72nd Annual International Meeting of the Society of Exploration Geophysicists Expanded Technical Program Abstracts with Biographies*. Society of Exploration Geophysicists, Tulsa, OK, 512–515.
- Pitman, J.K. & Spencer, C.W. 1984. Petrology of selected sandstones in the MWX wells, (northwest Colorado) and its relationship to borehole geophysical-log analysis and reservoir quality. In: Spencer, C.W. & Keighin, C.W. (eds) *Geological Studies in Support of the U.S. Department of Energy Multiwell Experiment, Garfield County, Colorado*. United States Geological Survey, Open-File Report, **84-757**, 33–66.
- Pitman, J.K. & Sprunt, E.S. 1986. Origin and distribution of fractures in lower Tertiary and Upper Cretaceous rocks, Piceance Basin, Colorado, and their relation to the occurrence of hydrocarbons. In: *Geology of Tight Gas Reservoirs*. American Association of Petroleum Geologists, Studies in Geology, **24**, 221–233.
- Pranter, M.J. & Sommer, N.K. 2011. Static connectivity of fluvial sandstones in a lower coastal-plain setting: An example from the Upper Cretaceous lower Williams Fork Formation, Piceance Basin, Colorado. *American Association of Petroleum Geologists Bulletin*, **95**, 899–923.
- Pranter, M.J., Ellison, A.I., Cole, R.D. & Patterson, P.E. 2007. Analysis and modeling of intermediate-scale reservoir heterogeneity based on a fluvial point-bar outcrop analog, Williams Fork Formation, Piceance Basin, Colorado. *American Association of Petroleum Geologists Bulletin*, **91**, 1025–1051.
- Pranter, M.J., Vargas, M.F. & Davis, T.L. 2008. Characterization and 3-D reservoir modeling of fluvial sandstones of the Williams Fork Formation, Rulison Field, Piceance Basin, Colorado. *Journal of Geophysics and Engineering*, **5**, 158–172.
- Pranter, M.J., Cole, R.D., Panjaitan, H. & Sommer, N.K. 2009. Sandstone-body dimensions in a lower coastal-plain depositional setting; lower Williams Fork Formation, Coal Canyon, Piceance Basin, Colorado. *American Association of Petroleum Geologists Bulletin*, **93**, 1379–1401.
- Sava, D., Mavko, G. & Sayers, C.M. 2007. Rock physics-based integration of geological and geophysical data for fracture characterization; fractures. *Leading Edge*, **26**, 1140–1146.
- Schoenberg, M.S. & Douma, J. 1988. Elastic wave propagation in media with parallel fractures and aligned cracks. *Geophysical Prospecting*, **36**, 571–590.
- Shaak, R.V. 2010. *Stratigraphic architecture of shallow-marine to coastal-plain parasequences: Lower Williams Fork Formation, southeastern Piceance Basin, Colorado*. MS thesis, University of Colorado. Boulder, CO.
- Spencer, C.W. 1996. Uinta–Piceance Province (020). In: Gautier, D.L., Dolton, G.L., Takahashi, K.I. & Varnes, K.L. (eds) *1995 National Assessment of United States Oil and Gas Resources – Results, Methodology, and Supporting Data*. United States Geological Survey, Digital Data Series, **DDS-30**, Release, **2**, 1 (CD-ROM).
- Tezuka, K., Namikawa, T., Tamagawa, T., Day-Lewis, A. & Barton, C.A. 2002. Roles of the fracture system and state of stress for gas production from the basement reservoir in Hokkaido, Japan. In: *SPE Gas Technology Symposium, 30 April–2 May 2002, Calgary, Alberta, Canada*. Society of Petroleum Engineers, Richardson, TX, SPE Paper 75704.
- Tremain, C.M. 1993. Chapter PC-2—Mesaverde Group. In: Hjellming, C.A. (ed.) *Atlas of Major Rocky Mountain Gas Reservoirs*. New Mexico Bureau of Mines and Mineral Resources, Socorro, NM, 97–98.
- Tweto, O. 1975. Laramide (Late Cretaceous-early Tertiary) orogeny in the southern Rocky Mountains. In: Curtis, B.F. (ed.) *Cenozoic History of the Southern Rocky Mountains*. Geological Society of America, Memoirs, **144**, 1–44.
- Verbeek, E.R. & Grout, M.A. 1984. *Fracture Studies in Cretaceous and Paleocene Strata in and around the Piceance Basin, Colorado; Preliminary Results and their Bearing on a Fracture-Controlled Natural-Gas Reservoir at the MWX Site*. United States Geological Survey, Open-File Report, **OF 84-0156**.
- Williams, G.D., Powell, C.M. & Cooper, M.A. 1989. Geometry and kinematics of inversion tectonics. In: Cooper, M.A. & Williams, G.D. (eds) *Inversion Tectonics*. Geological Society, London, Special Publications, **44**, 3–15.